Diffuse scattering from dynamically compressed single-crystal zirconium following the pressure-induced $\alpha \rightarrow \omega$ phase transition

P. G. Heighway [1,*] S. Singh [2] M. G. Gorman,[2] D. McGonegle [3,4] J. H. Eggert [2] and R. F. Smith [2]

[1]*Department of Physics, Clarendon Laboratory, University of Oxford, Oxford OX1 3PU, United Kingdom*

[2]*Lawrence Livermore National Laboratory, Livermore, California 94550, USA*

[3]*AWE, Aldermaston, Reading RG7 4PR, United Kingdom*

[4]*Oxford Centre for High Energy Density Science, Department of Physics, Clarendon Laboratory, University of Oxford, Oxford OX1 3PU, United Kingdom*

(Received 30 April 2024; revised 4 July 2024; accepted 8 July 2024; published 27 August 2024)

The prototypical $\alpha \rightarrow \omega$ phase transition in zirconium is an ideal test bed for our understanding of polymorphism under extreme loading conditions. After half a century of study, a consensus had emerged that the transition is realized via one of two distinct displacive mechanisms, depending on the nature of the compression path. However, recent dynamic-compression experiments equipped with *in situ* diffraction diagnostics performed in the past few years have revealed new transition mechanisms, demonstrating that our understanding of the underlying atomistic dynamics and transition kinetics is in fact far from complete. We present classical molecular dynamics simulations of the $\alpha \rightarrow \omega$ phase transition in single-crystal zirconium shock compressed along the [0001] axis using a machine-learning-class potential. The transition is predicted to proceed primarily via a modified version of the two-stage Usikov-Zilberstein mechanism, whereby the high-pressure ω phase heterogeneously nucleates at boundaries between grains of an intermediate β phase. We further observe the fomentation of atomistic disorder at the junctions between β grains, leading to the formation of highly defective interstitial material between the ω grains. We directly compare synthetic x-ray diffraction patterns generated from our simulations with those obtained using femtosecond diffraction in recent dynamic-compression experiments, and show that the simulations produce the same unique, anisotropic diffuse scattering signal unlike any previously seen from an elemental metal. Our simulations suggest that the diffuse signal arises from a combination of thermal diffuse scattering, nanoparticlelike scattering from residual kinetically stabilized α and β grains, and scattering from interstitial defective structures.

DOI: 10.1103/PhysRevB.110.054113

I. INTRODUCTION

When dynamically compressed to planetary pressures and temperatures, even the most apparently simple elements can exhibit rich allotropy. Among the best-known examples are the group-XI metals Cu, Ag, and Au, all of which undergo a face-centered-cubic (fcc) to body-centered-cubic (bcc) phase transition at just under 200 GPa [1–4]; the group-IV metals Ti, Zr, and Hf, which follow a hexagonal-close-packed (hcp) to simple hexagonal (hex-3) to bcc transition path over a few tens of gigapascals [5,6]; the group-XIV semiconductor Si, which experiences three phase transitions along the Hugoniot before shock melting at just 27 GPa [7–10]; and its congener C, whose elusive BC8 "superdiamond" phase transition at 1 TPa remains the subject of intense investigation [11–13]. With the worldwide proliferation of high-power, long-pulse laser-compression platforms that allow us to shock or ramp compress solid targets rapidly and reproducibly to gigapascal-scale pressure states, coupled to ultrafast x-ray diagnostics that capture transformations of their crystal structure *in situ* within the nanosecond window before they disintegrate, the experimental observation of polymorphism under extreme loading conditions has become almost routine. The study of pressure-induced polymorphism informs our understanding of condensed matter physics at its most fundamental level, and at a rate that will only increase in the coming decade with the arrival of high-repetition-rate instruments such as the DiPOLE 100-X laser at the European X-ray Free-Electron Laser (EuXFEL) [14].

With the high-pressure phase diagrams of many important elements now firmly established (along the Hugoniot, at least), the focus of current phase-transition studies is shifting towards the identification of the atomistic mechanisms by which transformations are realized. Displacive solid-solid phase transitions are characterized by a unique atomistic pathway, each of which brings about a high-pressure daughter phase with a particular orientation relationship (OR) with the ambient parent phase. The orientation of the daughter phase is readily deduced from the azimuthal angles at which its diffraction peaks do or do not appear, while the orientation of the parent phase is often known in advance by virtue of the target being a single crystal. Experimentally determined ORs have successfully been used to discriminate between rivaling

*Contact author: patrick.heighway@physics.ox.ac.uk

atomistic transformation mechanisms in Fe [15], Si [16], Cu [17], and Zr [18]. Studies offering this depth of analysis are currently rare, but are absolutely essential to developing our understanding of the lattice-level dynamics associated with solid-solid phase transitions.

The nature of the $\alpha \rightarrow \omega$ (hcp $\rightarrow$ hex-3) transition in zirconium is arguably the most complex and contentious of any elemental metal. Decades of experimental study have revealed that the ductile-to-brittle $\alpha \rightarrow \omega$ phase transition is generally realized via one of two inequivalent mechanisms. The first yields an ω phase that assumes the so-called TAO-I OR with the parent α crystal, and is usually observed in samples recovered from uniaxial shock-compression scenarios [19–21]. The second mechanism produces an ω phase that takes the Silcock OR, and is more often observed during static compression or under high-pressure torsion [22–27]. These trends do not hold universally, however: in several instances the "converse" mechanism has been observed [28,29], and, in a dynamic-compression study by Swinburne *et al.*, the authors reported an entirely new OR [30] (the interpretation of which was questioned soon thereafter in Ref. [31]). The situation became yet more complicated following a very recent experimental-computational study by Singh *et al.* [18]. Using femtosecond x-ray diffraction to characterize the $\alpha \rightarrow \omega$ phase transition in single-crystal Zr shock compressed along its [0001] direction, the authors measured three distinct ORs *simultaneously* (namely, the TAO-I, the Silcock, and another previously unreported OR), demonstrating that the $\alpha \rightarrow \omega$ transition was being realized via three competing, concurrent mechanisms. No single account of the phase-transition kinetics in Zr yet exists that harmonizes these seemingly disparate results; clearly, there is still a great deal to be learned about (and from) high-pressure polymorphism in zirconium.

In addition to the multiple competing $\alpha \rightarrow \omega$ transition mechanisms, Singh *et al.* observed a second curious feature in the data: a diffuse scattering signal of comparable total intensity to the Bragg peaks that exhibited a pronounced, sixfold-symmetric structure around the beam direction. The diffuse signal would appear to suggest atomistic disordering of some description, but its azimuthal structure rules out a simple isotropic liquid or glass. In that previous study [18], the authors briefly presented the results of classical molecular dynamics (MD) simulations of shock-compressed, [0001]-oriented Zr single crystals that reproduced the same diffuse, azimuthally structured diffraction signal, but did not discuss its source. The purpose of this study is to describe the aforementioned MD simulation campaign in complete detail. We will examine the rich and complex microstructural evolution precipitated by the $\alpha \rightarrow \omega$ phase transition, focusing on the displacive and diffusive mechanisms through which the transition is realized. We will then interrogate the reciprocal-space structure of the shock-loaded system, and make direct comparisons between experimental and synthetic diffraction signals. By combining these real- and reciprocal-space analyses, we will explain the origin of the unique diffuse scattering signal measured experimentally by Singh *et al.* [18].

The paper is laid out as follows. We first give a detailed description of our simulation methodology in Sec. II, including details of the interatomic potential used, the shock-compression technique, and the characterization techniques employed. The results of the simulations are given in Sec. III, which is subdivided into real-space (Sec. III A) and reciprocal-space (Sec. III B) analyses. We then discuss the implications of our results in Sec. IV before concluding in Sec. V.

II. METHODOLOGY

A. Interatomic potential

The choice of the classical potential governing the microscopic forces exerted between atoms, and from which all the resulting mesoscale and macroscale physics flows, is the linchpin of any simulation campaign. Since no classical potential is universally transferable, one must choose from those available the potential that best captures the most pertinent physics. To faithfully model the pressure-induced $\alpha \rightarrow \omega$ phase transition in shock-loaded zirconium, we require the following of our potential: (1) that it correctly predict the high-pressure phase diagram of Zr; (2) that it reproduce the energy variation along the transition pathways between these phases; and (3) that it yield a reasonably accurate Hugoniot. The potential must also be computationally efficient enough to permit access to the "large" spatiotemporal scales of grain nucleation, growth, and coalescence. Taken together, these constraints leave perhaps only three Zr potentials [35–37] suitable for these high-pressure conditions.

From these viable potentials, we have selected the machine-learning-class potential developed by Zong *et al.* [35] (hereafter referred to as the Zong potential). In contrast to simpler, physically motivated potentials like those of the widely used embedded-atom-method (EAM) family, the Zong potential (and other machine-learning potentials like it [38–41]) employ a complex and largely abstract parametrization scheme that affords them greater flexibility. In brief, the energy of each atom is expressed as a function of a set of unique configurational 'fingerprints' distilled from its local bonding environment. The function that maps the local fingerprints onto a per-atom energy is constructed by training the potential on a multiphase energy database generated from *ab initio* molecular dynamics (AIMD) simulations. This potential was tailored to reproduce the high-pressure allotropy of zirconium that we seek to model here, and has the added benefit of having already been tested in shock-loading scenarios [42,43], meaning we have previous results against which to benchmark our own.

As we show in Fig. 1, the Zong potential largely succeeds in reproducing the experimentally measured [32] hydrostatic phase boundaries between the α, β, and ω phases of Zr at high pressures. Its idealized Hugoniot in pressure-temperature space (the calculation of which is described in the Supplemental Material [44]) also follows closely the locus of shock states predicted by the Multiphase equation of state (EOS) of Greeff [33]. The MD-simulated shock state we focus on here (which sits marginally above the idealized Hugoniot) lives deep in the ω-stability region where the potential performs best. A comprehensive assessment of the Zong potential's performance against experimental and AIMD benchmarks can be found in Ref. [45].

We note that there is a drawback to the relatively flexible nature of the Zong potential: there exist isolated pockets of configuration space over which its energy surface changes

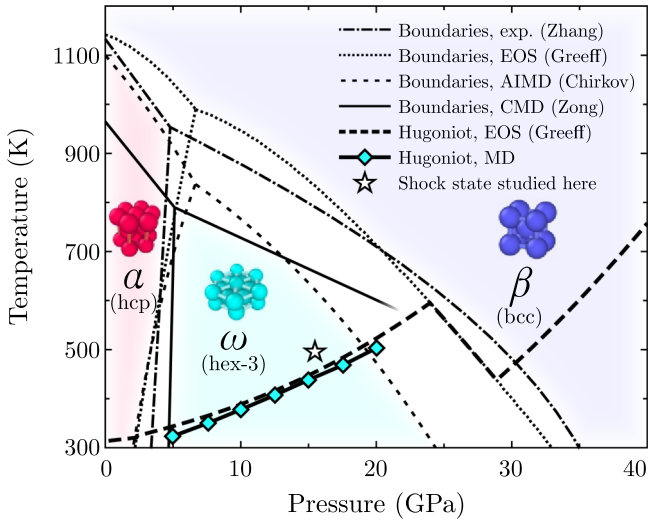

FIG. 1. Hydrostatic high-pressure phase diagram and principal Hugoniot of zirconium. Shown are phase boundaries between the α (hcp), β (bcc), and ω (hex-3) phases determined in cubic-anvil-based experiments by Zhang *et al.* [32], from a three-phase, semiempirical equation of state (EOS) by Greeff [33], *ab initio* molecular dynamics (AIMD) calculations by Chirkov [34], and from classical MD (CMD) simulations conducted with the Zong potential [35]. Also shown is the Hugoniot from the Greeff EOS and from the Zong potential, the latter being approximated by solving the Rankine-Hugoniot equation $E - E_0 = \frac{1}{2}P(V_0 - V)$ for a perfect ω single crystal. The shock state examined here is marked by a star.

discontinuously. This fact does not appear to be widely known: we are aware of only one other study documenting it, namely, a recent systematic comparison of 13 Zr potentials by Nicholls *et al.* [45]. The effect of these discontinuities is twofold: first, atoms sporadically experience moderately elevated forces for short, 10-fs bursts every few hundred picoseconds (an example trajectory can be found in the Supplemental Material [44]); second, truncation errors from the finite simulation time step (1 fs) accumulate quickly enough that the system's total mechanical energy steadily drifts over $\sim$0.1 ns timescales, meaning the evolution of the system is nonadiabatic. We can mitigate the latter problem by applying a gentle global thermostat that absorbs artificially generated heat, but this does not address the underlying issue of spurious atomic forces.

However, we will demonstrate that, despite its apparent shortcomings, simulations conducted under the Zong potential reproduce most of the salient features of experimental diffraction data taken from zirconium shock compressed along [0001]. That is, we do not need to rely on *ab initio* validation of the potential as many (perhaps most) similar MD-based dynamic-compression studies do, but can instead verify the potential directly using like-for-like comparisons of synthetic and experimental x-ray diffraction patterns. The prevailing agreement between the two indicates that the Zong potential's discontinuities do not significantly impede its ability to make realistic physical predictions.

B. Simulation setup

Our molecular dynamics simulations largely follow the conventional template for modeling single crystals under uniaxial compression. The crystals we simulate are initially defect-free blocks of α-Zr with their $[2\bar{1}\bar{1}0]$, $[01\bar{1}0]$, and [0001] directions aligned with the x, y, and z axes of the computational cell, respectively. The presence of laterally confining material surrounding the computational cell is imitated by the application of periodic boundary conditions (PBCs) in the x and y directions. Crystals span 40 nm in the transverse directions, which is more than sufficient to prevent nascent grains of the high-pressure ω phase interacting with periodic images of themselves at late times. Shock waves are launched by driving a momentum mirror into the lower xy face of the crystal from rest to a final velocity of $U_P = 0.54$ kms^{-1} (yielding a shock pressure of around 15 GPa) over a period of 0.8 ps (the rise time of the elastic precursor wavefront at this pressure). A simulation time step of 1 fs is used throughout. All simulations are executed with the LAMMPS code [46]; the Zong potential requires that we use the December 2014 release to ensure compatibility.

The Zong potential is around two orders of magnitude more expensive per atom time step than the workhorse EAM potentials commonly used in multimillion-atom shock simulations. Indeed, its cost is so great that the naive approach to shock MD, wherein a thick target is constructed with its final desired dimensions from the outset of the simulation, is not only woefully inefficient, but also so expensive as to make an extended simulation campaign prohibitively unwieldy, even using supercomputing facilities. To make the campaign tractable, we need to reduce the simulation size without compromising the structure of the shock. Several modified integration schemes have been developed, such as the Hugoniostat [47] and multiscale shock technique (MSST) [48], that impose uniaxial strain on a relatively small, homogeneous atomistic system in such a way as to respect the Rankine-Hugoniot jump conditions, thus eliminating the need for the large "runway" of material used in conventional shock-MD simulations. However, these schemes require the user to choose hyperparameters that influence the relaxation process and thus partially control the microstructure generated by the shock. Here, we use an alternative two-stage scheme similar in spirit to the moving-window technique [49] that allows us to efficiently simulate shock compression without the need to specify external parameters. We refer to our approach as the "grow-and-prune" scheme, which is illustrated in Fig. 2.

At the start of the simulation, there exists a sliver of α-Zr spanning the full 40×40 nm^2 transverse extent of the cell, but extending only 9 nm in the shock direction. During stage I of the simulation, we "grow" the crystal along the compression direction by iteratively appending new material to its rear surface at a rate commensurate with the shock speed. A growth event is triggered when the foot of the leading shock front comes within distance $\delta = U_S^e \Delta t_{\text{eq}}$ of the crystal's rear surface, where U_S^e is the speed of the elastic precursor wave and $\Delta t_{\text{eq}} \approx 1$ ps is the time required for a pristine crystal to thermalize. We detect the arrival of the shock by evaluating the center-of-mass velocity of a sliver of material a distance δ from the rear surface every 0.2 ps and checking if its value exceeds 50% of the driving mirror velocity U_p. If it does, we append a new sliver of α-Zr of thickness δ to the rear surface; the fresh material is able to equilibrate for time Δt_{eq} before the shock front reaches it. By building the runway needed for the

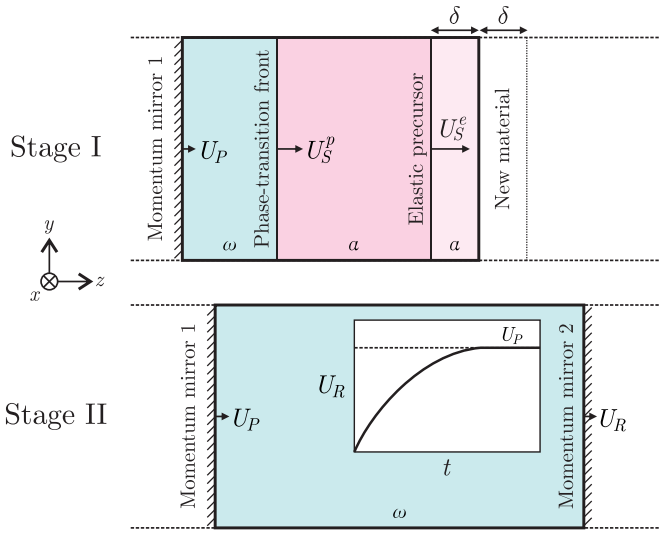

FIG. 2. Depiction of the grow-and-prune scheme used to conduct simulations of uniaxial shock compression. In stage I, a momentum mirror with speed U_P drives a two-wave structure with an elastic precursor traveling at speed U_S^e. The crystal emerging from the mirror "grows" over the simulation; when the precursor wave comes within distance δ of the rear surface, the crystal is extended by the addition of fresh material of thickness δ. At the start of stage II, material beyond a specified cutoff is deleted ("pruned"). The remaining block of mostly compressed material nearest the first momentum mirror is isolated and its rear surface pressurized by a second momentum mirror traveling at speed $U_R \leqslant U_P$. The inset illustrates the time variation of U_R, which slowly approaches and eventually saturates at the particle velocity U_P.

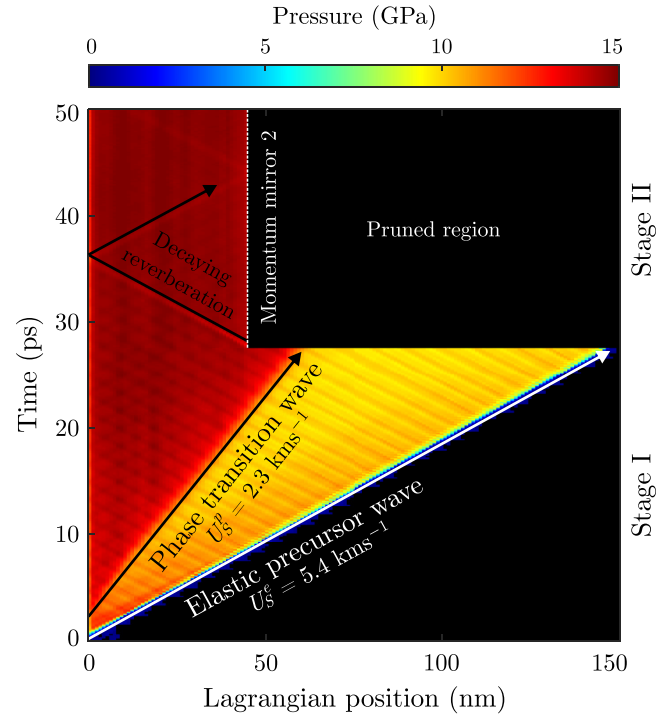

FIG. 3. Spatiotemporal evolution of the pressure in single-crystal α-Zr shock compressed along [0001] with a momentum mirror traveling at 0.54 kms^{-1}, modeled using the Zong potential [35]. New material is iteratively appended to the rear surface of the crystal to keep pace with the elastic precursor wave traveling at 5.4 kms^{-1}. At $t = 27.5$ ps, material beyond $z_L = 45$ nm is removed, and a second momentum mirror is installed at the crystal's new rear surface to keep the remaining material pressurized. Regions in which no material exists are rendered as black in this color scheme.

shock in this iterative manner, we avoid needless simulation of ambient material distant from the shock front and approximately double our computational efficiency.

Once a sufficiently large and uniform body of compressed material has accumulated behind the shock, we select all atoms beyond this chosen region and remove them from the simulation; we refer to this as "pruning." For the present simulation, this occurs after 30 growth events, each of which appends $\delta = 4.7$ nm of new material onto the crystal; when we prune, we reduce the (Lagrangian) length of the crystal from 150 nm to just under 50 nm. At the new free surface of the cell, we construct a second momentum mirror whose initial velocity $U_R(t_I)$ matches the local particle velocity of the rear surface. To disturb the wave structure as little as possible, we fit the time variation of the particle velocity following the onset of the $\alpha \rightarrow \omega$ phase transition to a phenomenological sigmoid function, and then vary U_R according to this function until it reaches the final particle velocity U_P, after which time we cap the second mirror's velocity:

$$U_R(t) = \min\left[U_0 + \Delta U\left(\frac{\frac{t-t_0}{\Delta t_{\text{front}}}}{1+\left|\frac{t-t_0}{\Delta t_{\text{front}}}\right|}\right), U_P\right]. \qquad (1)$$

The fitting process and parameters are shown in the Supplemental Material [44]. Once the second momentum mirror reaches speed U_P, the two mirrors confining the remaining material travel at identical speeds and thus impose constant-volume conditions. The pruning step allows us to efficiently study slow, postshock microstructural evolution at late times (hundreds of picoseconds after the shock) without needing to continue to simulate the shock wave itself.

To demonstrate the grow-and-prune technique, we show in Fig. 3 the structure of the pressure waves generated in our Zr shock-compression simulation. We observe a two-wave structure, with an elastic precursor wave traveling at $U_S^e = 5.4$ kms^{-1} trailed by a phase-transition wave with velocity $U_S^p = 2.3$ kms^{-1}. Note that, during stage I, successive crystal-growth events generate a train of weak stress waves that propagate back towards and eventually reflect from the front surface, leading to the conspicuous cross-hatch pattern visible in the region behind the phase-transition front. The magnitude of the pressure modulations amounts to no more than $\pm 2.5\%$ of the local, time-averaged pressure, which we believe is too small to substantively change the dynamic response of the crystal. Indeed, we have verified that the behavior of Zr crystals simulated using a relatively inexpensive EAM potential [50] with and without the iterative construction scheme are essentially identical (see Supplemental Material [44]). We also note the presence of a reverberation of magnitude $\sim$0.8 GPa emitted at the beginning of stage II; it is difficult to eliminate the small velocity discontinuity introduced by the second momentum mirror entirely. However, the reverberation is unsupported and decays quickly, and is therefore unlikely to significantly change the microstructure of the final Hugoniot state.

The dynamic stage I of our simulations lasts 27.5 ps, while the quasistatic stage II lasts a further 172.5 ps. During the latter stage, we apply a Nosé-Hoover thermostat with a target temperature of 500 K (the average system temperature at the end of stage I) and a damping time of 5 ps, which is just sufficient to arrest the slow temperature drift caused by the artificially generated heat discussed in Sec. II A. The final shocked configuration we focus on here is thus found in the pressure-temperature state (15 GPa, 500 K), which lies close to the theoretical Hugoniot (see Fig. 1).

We estimate (see Supplemental Material [44]) that the grow-and-prune technique saves us a factor of 8 in computational costs, reducing the number of atoms we need to simulate from 7.5×10^7 to no more than 1×10^7. Without it, the cost of the Zong potential, or other machine-learning-class potentials like it, would render this simulation campaign unworkable.

C. Characterization techniques

To characterize the real-space structure of the simulated atomistic configurations, we use a range of both standard and tailored coordination analysis techniques. The most important step in the workflow is the initial partitioning of the configuration into α (hcp), β (bcc), ω (hex-3), and noncrystalline structures. In brief, the partitioning is realized in two steps. We first identify atoms in the ω phase with the Ackland-Jones parameter (AJP) [51] using a modified version of the original approach taken by Zong *et al.* [42]. We then classify the remaining atoms according to adaptive common-neighbor analysis (a-CNA) [52]. We give a detailed description of the full algorithm in the Supplemental Material [44]. Note that we always perform the partitioning using atomic coordinates that have been time averaged over 200 fs in order to combat thermal fluctuations, which degrade the accuracy of the structure classification.

To characterize the orientation of incipient crystal structures, we employ two different techniques. We measure the rotation (and elastic strain) state of the β phase using the relatively computationally cheap template-matching technique (TMT) described in Ref. [53], whereby each atom's unit cell is assigned to one of a set of candidate unit cells based on the similarity of their orientations. For atoms in the ω phase (to which the TMT technique has not yet been extended), we instead use the per-atom structure factor (PASF) defined in Ref. [54], the structure factor of a small spherical cluster of atoms surrounding the central atom. Originally used to discriminate between different twin variants in bcc tantalum, here we use the PASF to distinguish ω grains with different orientation relationships with the original α crystal.

To synthesize diffraction patterns from the simulated atomistic configurations, we first obtain the raw ionic structure factor using the standard expression

$$S(\mathbf{q}) = \left| \sum_{\alpha=1}^{N} e^{-i\mathbf{q}\cdot\mathbf{r}_\alpha} \right|^2, \tag{2}$$

where $\mathbf{r}_\alpha$ is the instantaneous position of atom α. We then sample the structure factor on the spherical locus of q vectors constituting the Ewald sphere, and postmultiply the resultant intensity by the atomic-form, polarization, and self-attenuation factors. Note that whenever we calculate synthetic diffraction patterns from the late-time atomistic configuration, we Fourier transform not the entire cuboidal computational cell, but the inscribed sphere of atoms it contains. We do this to remove the hard, flat edges of grains at the edge of the box that would otherwise generate sharp, artificial, sinclike features in reciprocal space.

III. RESULTS

Our results are separated into real- and reciprocal-space analyses. The real-space analysis (Sec. III A) focuses on the atomistic mechanisms by which the $\alpha \rightarrow \omega$ transition is realized and the complex microstructure that results. The reciprocal-space analysis (Sec. III B) explores this microstructure's x-ray diffraction signatures, both crystalline and diffuse, and compares these features with those observed in femtosecond diffraction experiments on shock-compressed Zr.

A. Real-space analysis

We begin by examining the gross structure of the shock wave. Shown in Fig. 4 is an atomistic visualization of the shock-compressed Zr crystal after 27.5 ps, at the end of stage I of the simulation. At this instant, the computational cell is at its maximum extent (containing some 10 million atoms) and the two-wave structure has had time enough to fully develop. We color atoms by both their local pressure and crystal structure to correlate the wave structure with the underlying microstructural evolution.

An elastic precursor wave traveling at 5.4 kms^{-1} leads the shock, elevating the pressure to 10 GPa while preserving an α (hcp) crystal structure. The phase-transition front pursues the precursor wave at 2.3 kms^{-1}, and further raises the pressure to its final value of 15 GPa. Figure 4 reveals that the material behind the $\alpha \rightarrow \omega$ transition front possesses a rich, diverse microstructure comprising not only nanocrystals of the high-pressure ω phase, but also pockets of metastable β- (bcc-)Zr, in addition to swathes of interstitial noncrystalline matter. Our first objective is to identify the lattice-level mechanisms that create this complex configuration. It transpires that the short-lived β phase, an intermediate between the α and ω phases, is absolutely essential to the formation of the rich microstructure we observe.

To better understand the postshock phase dynamics, we show in Fig. 5 the evolution of the local mass fractions of the α, β, ω, and noncrystalline structures following the arrival of the phase-transition front. The parent α phase rapidly diminishes over a few picoseconds, and is initially replaced not by the ω phase, but the β. The nascent β phase reaches its maximum mass fraction after just 10 ps, before decaying at the expense of a growing ω phase, whose population eventually saturates at just over 60% of the crystal after 200 ps. The residual isolated clusters of untransformed α- and β-Zr constitute only 2% and 5% of the late-time atomistic configuration, respectively. The remaining 33% of the atoms assume noncrystalline structures. The majority of these atoms are situated on grain boundaries, but some form volumetric disordered nanoclusters sitting in the interstices between ω grains (as

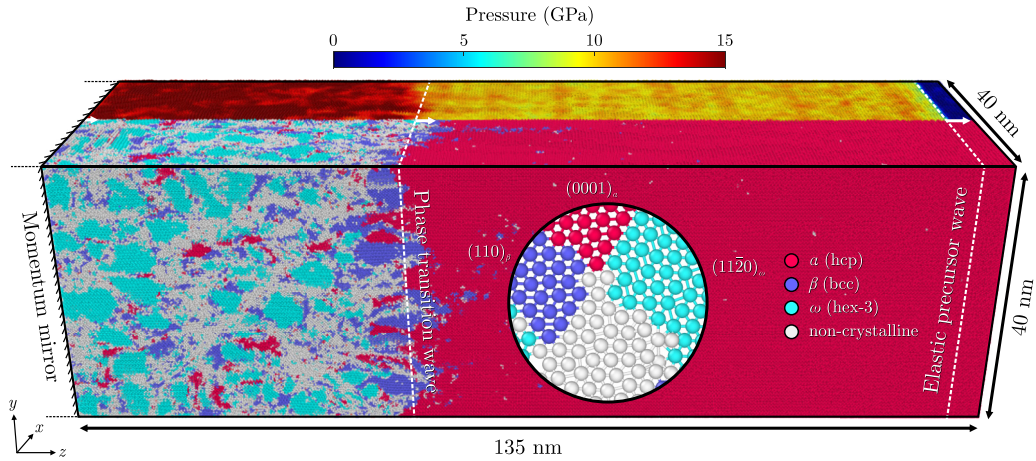

FIG. 4. Visualization of single-crystal Zr modeled under the Zong potential [35] shock compressed along its [0001] axis to 15 GPa using a momentum mirror with velocity $U_P = 0.54$ kms^{-1}. Foreground atoms are colored according to their local crystal structure, with α, β, ω, and noncrystalline environments rendered in magenta, blue, cyan, and gray, respectively. The inset shows a closeup of an intersection between the four structures viewed in a plane orthogonal to the shock. Atoms at the back of the cell are colored by their local pressure. This and all other visualizations were rendered in OVITO [55].

will be discussed later). The most important conclusion to be drawn from Fig. 5 is that there exists a brief but clearly defined "β epoch" during which the bcc phase is the dominant extant crystal structure. We will now examine the $\alpha \rightarrow \beta \rightarrow \omega$ transition process in greater detail, and demonstrate the critical role the transient β nanocrystal plays in the formation of the ω and noncrystalline material.

The transition process unfolds in four stages, which are illustrated in Fig. 6. First, supercritical β nuclei form throughout the bulk of the uniaxially strained parent α crystal. The daughter nuclei undergo rapid, directional growth until they meet and form an extremely fine nanocrystalline aggregate. Only then do we observe the first appearance of ω nuclei. These (grand)daughter nuclei consume the β grains as they grow until they meet and coalesce, thus forming a relatively coarse ω nanocrystal with a characteristic grain size of around 6 nm.

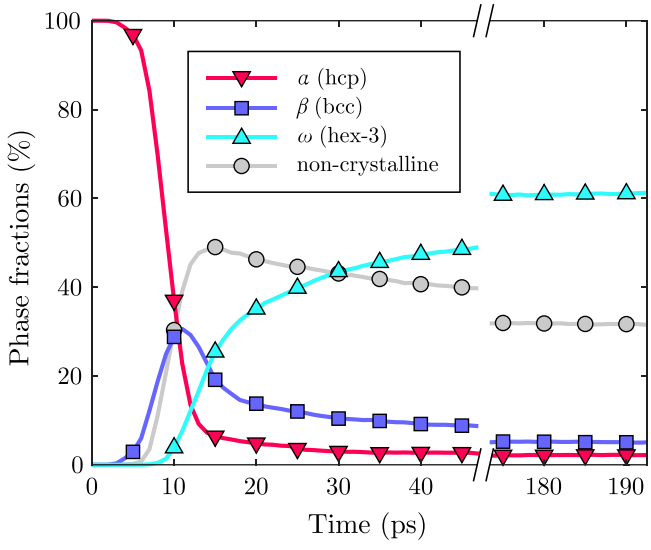

FIG. 5. Evolution of the α, β, ω, and noncrystalline mass fractions in shock-compressed Zr following the arrival of the $\alpha \rightarrow \omega$ phase-transition front at $t = 0$ ps. Calculations were performed on an 11-nm-thick Lagrangian material element containing 1×10^6 atoms. Early- and late-time evolution are separated by a break in the time axis.

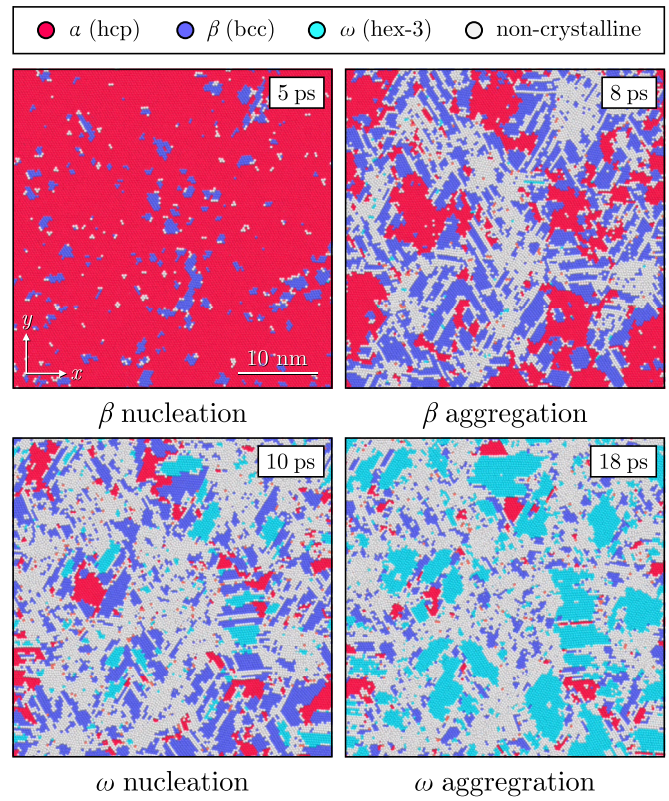

FIG. 6. Cross sections of single-crystal Zr shocked along [0001] to 15 GPa, with atoms visualized by local crystal structure. Snapshots taken 5, 8, 10, and 18 ps after the arrival of the phase-transition front, marking the four stages of the $\alpha \rightarrow \beta \rightarrow \omega$ transition.

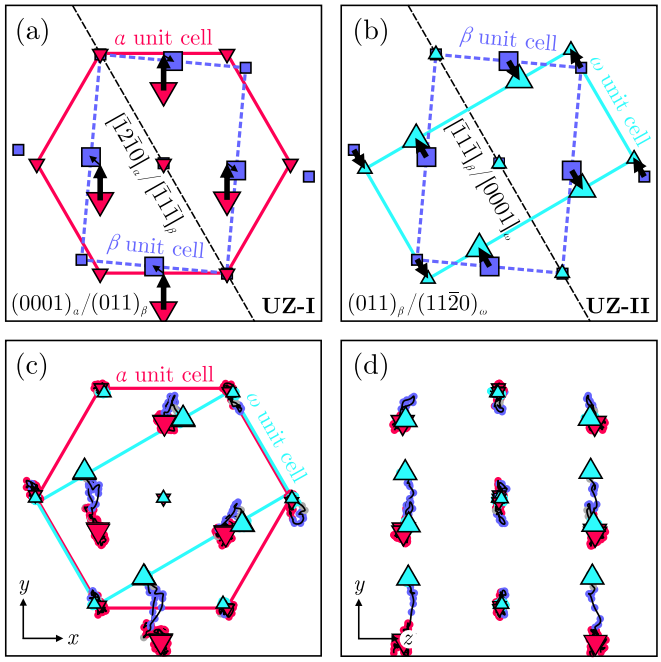

FIG. 7. Transformation of the Zr unit cell via the in-plane variant of the two-step Usikov-Zilberstein (UZ) pathway [28]. (a) Atomic motion during the first stage (UZ-I), where the $\alpha \rightarrow \beta$ transformation is realized by shuffling of alternating $(0001)_\alpha$ planes in the $\pm[01\bar{1}0]_\alpha$ directions (indicated by black arrows). Atoms in different $(0001)_\alpha/(011)_\beta$ planes are distinguished by different marker sizes. (b) Atomic motion during the second stage (UZ-II), whereby the $\beta \rightarrow \omega$ transformation is accomplished by shuffling of successive $(\bar{2}\bar{1}1)_\beta$ planes along the $\pm[\bar{1}1\bar{1}]_\beta$ directions. (c) A typical trajectory in our shock MD simulations, projected onto the xy plane. Circular markers show atomic positions in the unit cell color coded according to the instantaneous crystal structure of the cell; black traces have been added to make the trajectories more apparent. Larger markers indicate the time-averaged atomic positions during periods when the cell assumes α and ω structures. (d) The same trajectories projected onto the yz plane.

We have confirmed the prediction of this potential's authors [42] that under the high-shear-stress conditions of uniaxial shock compression, the $\alpha \rightarrow \omega$ phase transition is realized almost exclusively by the "in-plane" variant of the Usikov-Zilberstein (UZ) mechanism [28]. The two stages of this mechanism are illustrated in Figs. 7(a) and 7(b). The first stage (UZ-I) involves alternating $(0001)_\alpha$ planes shuffling along the $\pm[01\bar{1}0]_\alpha$ directions (along with modest compatibility shear and rotation) to convert α-Zr to β-Zr via the Burgers mechanism. The second stage (UZ-II) sees the $\beta \rightarrow \omega$ transformation accomplished by shuffles along $\langle 111\rangle_\beta$ directions orthogonal to the shock. In Figs. 7(c) and 7(d) we track the actual trajectories of the neighbors of an atom situated in a representative ω grain from our shock-MD simulation. The atomistic pathway they follow is identical, demonstrating that the dominant grain-growth mechanism is indeed the conventional in-plane UZ mechanism.

However, the mechanism by which the majority of the ω grains *nucleate* is subtly different. To understand the nucleation process, we must first characterize the β nanocrystal in which it unfolds. The symmetry of the Burgers mechanism by which the β phase homogeneously nucleates is such that each β grain can assume one of six orientations with respect to the parent α crystal [56]. The six orientations fall into three pairs of very similar orientations that we will not distinguish between, in order to simplify the discussion. The β grains can thus be thought of as assuming three distinct orientations, all of which have their $(011)_\beta$ plane normal parallel to $(0001)_\alpha$ (i.e., the shock direction z), but which are related to one another by rotations of 120° around z. We show on the left of Fig. 8 a visualization of the β grains at the instant when the β phase is most populous, with grains colored according to which of the three orientation relationships (ORs) they take with respect to the α crystal. We observe that β grains with dissimilar crystallographic orientations form a dense, interlocking structure with conspicuously straight boundaries that make angles of 0°, 120°, or 240° with the $[2\bar{1}\bar{1}0]_\alpha$ direction (the x axis).

Closer examination reveals that the grain boundaries are, in many cases, perfect $\{112\}_\beta$ twin boundaries (see inset of Fig. 8). This is a direct consequence of the symmetries of the Burgers mechanism, for which pairs of daughter β orientations constitute exact reflections of one another in the $\{112\}_\beta$ planes orthogonal to $[011]_\beta$. When we superimpose the loci traced out by these twin boundaries and the locations of nascent ω grains formed during the first few picoseconds after the β epoch (as we do on the right of Fig. 8) we see immediately that ω nucleation takes place preferentially on the twin boundaries between β grains. That is to say that the ω phase nucleates *heterogeneously*. After a supercritical ω nucleus forms on a β twin boundary, it spreads into and consumes both β grains either side of the boundary, generating a relatively large ω grain with a single orientation. Almost nowhere do we observe homogeneous nucleation of a ω crystallite within the bulk of a β grain.

To explain how and why heterogeneous ω nucleation occurs, we have considered the modified atomistic pathway by which the $\beta \rightarrow \omega$ transition would have to take place at a twin boundary. As illustrated in Fig. 9, an ω crystal with the same orientation as that generated via the conventional UZ-II pathway can be formed on a coherent $(\bar{2}\bar{1}1)_\beta$ twin boundary by a simple reversal of direction of the $\pm[\bar{1}1\bar{1}]_\beta$ atomic shuffles at the $\{211\}_\beta$ twin boundary, i.e., at the same point where the $(\bar{2}\bar{1}1)_\beta$ stacking sequence reverses. We have directly compared the energy barriers acting against both the conventional and twin-modified variants of the UZ-II pathway using small-scale, static MD simulations of the supercells pictured in Fig. 9. Each supercell contains a fully periodic β-Zr crystal with an initial elastic strain state akin to that of the transient β nanocrystals observed in our shock-MD simulations. For the conventional UZ-II pathway, we observe that the metastable β state is separated from the stable ω state by only a modest potential energy barrier (5 meV) easily overcome by thermal fluctuations, as anticipated. By contrast, the twinned UZ-II pathway exhibits no energy barrier whatsoever; the β twin boundary is in fact *unstable* to a transformation to the ω structure. While these simulations neglect the interface energy associated with the ω nucleus, and thus underestimate the kinetic barrier in both cases, we believe they nevertheless account for the observation that the coherent twin boundaries

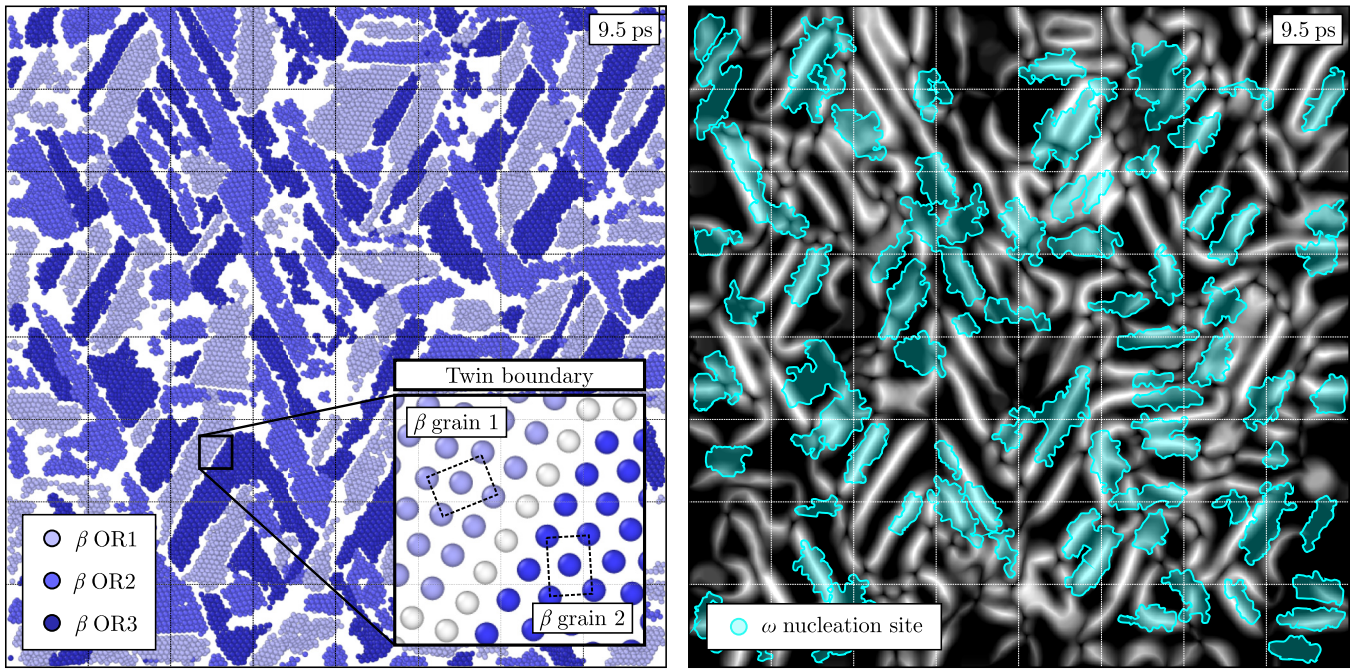

FIG. 8. Heterogeneous nucleation of the ω phase. (Left) β atoms in a 2-nm-thick cross section of the simulation cell, colored according to their approximate orientation relationship (OR) with the parent α crystal. Inset shows a coherent $\{112\}_\beta$ twin boundary between two β grains of differing ORs. Image taken at $t = 9.5$ ps, the height of the "β epoch." (Right) Locations of ω nuclei formed between 9.0 and 13.0 ps overlaid on a map highlighting boundaries between β grains at 9.5 ps.

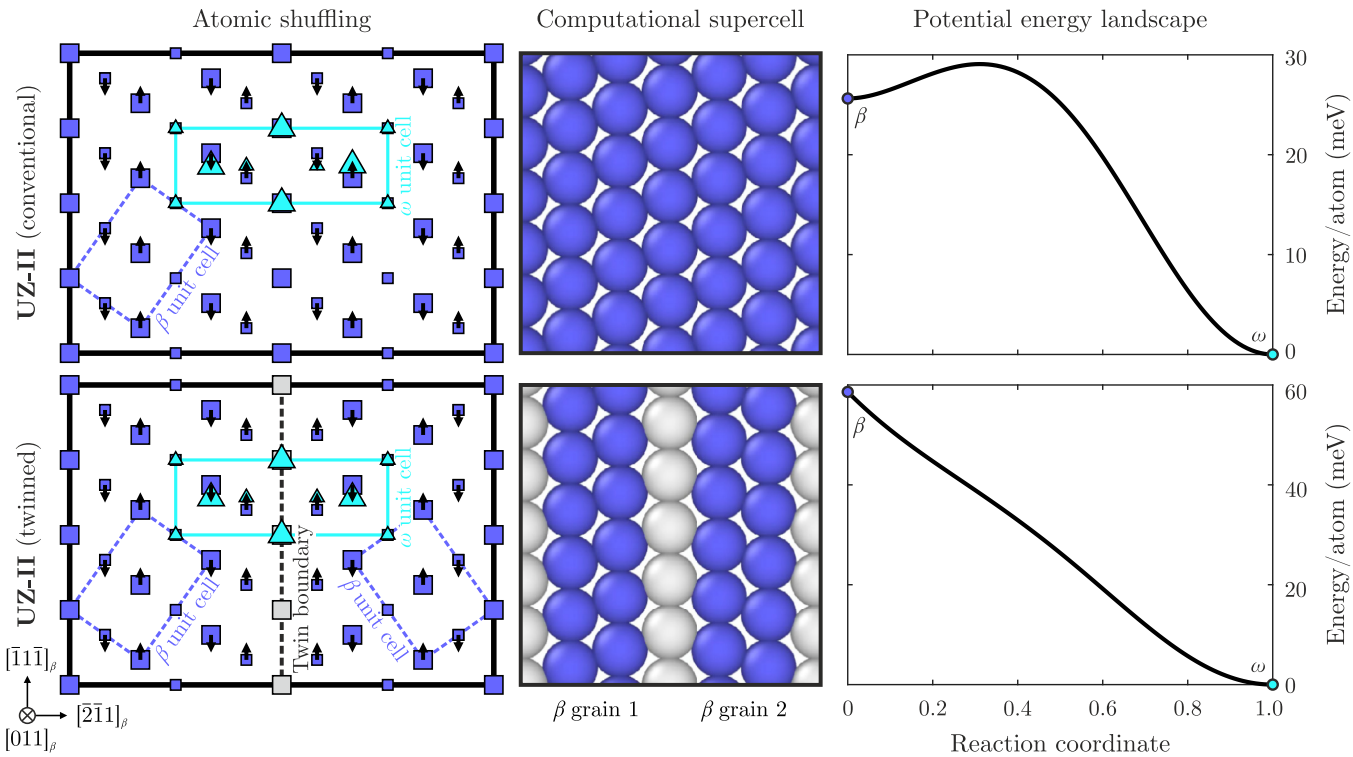

FIG. 9. Comparison of the conventional (top) and twinned (bottom) variants of the second stage of the Usikov-Zilberstein pathway (UZ-II) mediating the $\beta \rightarrow \omega$ transition. Left panes illustrate the necessary shuffling of successive $(\bar{2}\bar{1}1)_\beta$ planes in the $\pm[\bar{1}1\bar{1}]_\beta$ directions with and without the presence of a coherent $(112)_\beta$ grain boundary. Middle panes show initial cross sections of the prestressed supercell used to calculate the potential energy variation during UZ-II. Each fully periodic supercell contains 192 atoms, and is constructed with a cubic lattice constant of $a = 3.5$ Å and a compressive elastic strain of 7% along $[011]_\beta$ to approximate the strain state of the metastable β grains observed in shock-MD simulations. Right panels show the potential energy variation along each variant of the UZ-II pathway, defined with respect to the energy in the final ω state.

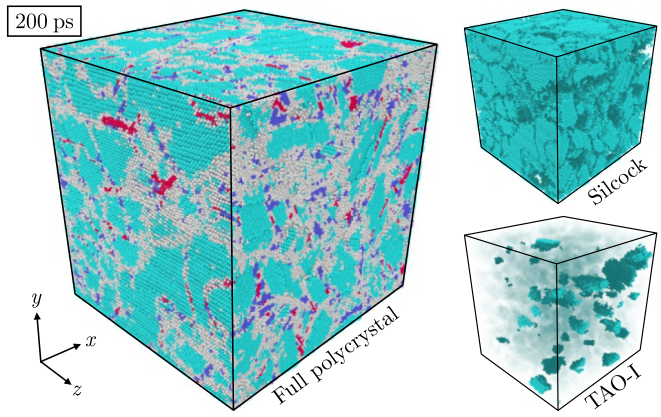

FIG. 10. Late-time (200-ps) decomposition of the ω grains (cyan) into those with the Silcock and the TAO-I orientations (formed by the in-plane and out-of-plane variants of the Usikov-Zilberstein mechanism, respectively) using the per-atom structure factor [54].

formed within the metastable β nanocrystal act as preferential nucleation sites for the ω phase.

We should note that while the in-plane UZ mechanism is dominant, we also observe a small proportion of ω grains that form via the "out-of-plane" variant, for which the UZ-II atomic shuffles take place in the $\langle 111\rangle_\beta$ directions with a component parallel to the shock, rather than those orthogonal to it. The ω material with final orientations consistent with the in-plane mechanism [the Silcock orientation [22] for which $(0001)_\alpha \parallel (11\bar{2}0)_\omega$ and $[\bar{1}2\bar{1}0]_\alpha \parallel [0001]_\omega$] and with orientations consistent with the out-of-plane mechanism [the TAO-I orientation [28] for which $(0001)_\alpha \parallel (01\bar{1}1)_\omega$ and $[11\bar{2}0]_\alpha \parallel [10\bar{1}1]_\omega$] constitute 95% and 5% of the late-time ω material, respectively. We show the morphology of the small and sparsely distributed TAO-I-oriented grains in Fig. 10. For comparison, in the experimental study of Singh *et al.* [18], the Silcock and TAO-I orientations, respectively, comprised 80% and 10% of the ω phase at 15 GPa, suggesting the Zong potential captures the transition kinetics for the two corresponding transition pathways reasonably well. However, we do not observe the third orientation detected by Singh *et al.* (dubbed variant-III), which comprised the remaining 10% of the ω-Zr. That the Zong potential fails to produce this third, previously unobserved pathway speaks to its lack of transferability (as commented upon in Ref. [45]).

Having studied the atomistic dynamics at the β twin boundaries, it is natural to ask the following: What happens at the *junctions* between β grains? It is here that we see the fomentation of atomistic disorder. In Fig. 11(a), we highlight regions of a representative cross section of the crystal in which atoms see at least one of their neighbors displaced by more than 3.5 Å (a distance comparable to the typical atomic separation) within the first 4 ps of the β nanocrystal reaching its maximum density. Such atoms cannot be participating in conventional displacive transition events like the UZ mechanism, but must instead be witnessing longer-range reordering of the kind seen in a diffusive transition. We observe that these diffusion sites preferentially appear at either incoherent, nonplanar boundaries between β grains, or at locations where several such grains converge, i.e., at locations where atoms are necessarily forced from the UZ pathway.

By the time the crystal approaches its late-time equilibrium state, the fraction of atoms that have participated in nondisplacive motion has grown considerably. We show in Fig. 11(b) a map of the average displacement experienced by each atom's original nearest neighbors over the crystal's cross section. Bodies of atoms that have undergone the regimented shuffling associated with the UZ mechanism are clearly marked out by their relatively small neighbor displacements, and by the equispaced striations that appear every third plane. Separating these bodies are veins of atoms whose average neighbor displacement is markedly greater. Approximately

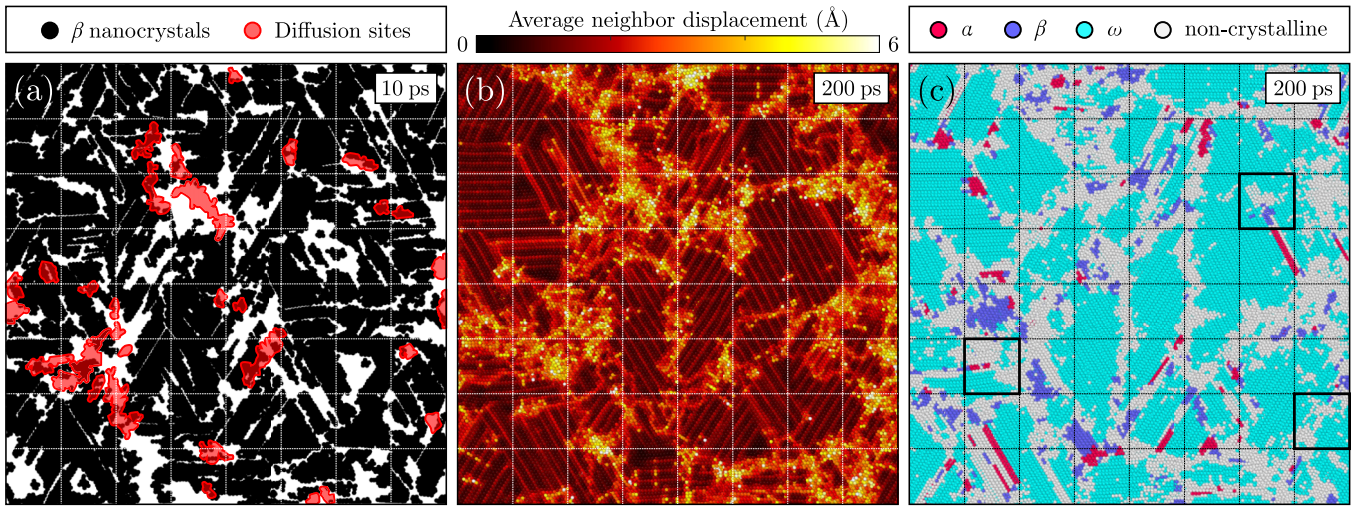

FIG. 11. Diffusive motion during the $\alpha \rightarrow \omega$ transition. (a) Locations of atoms at least one of whose neighbors move by more than 3.5 Å within the first 4 ps of the β nanocrystal aggregating, overlaid on a silhouette of β grains at 10 ps. (b) Late-time configuration of the same set of atoms colored according to the average displacement suffered by their neighbors, highlighting atoms that participate in nondisplacive motion. (c) The same atoms colored by their late-time local crystal structure. Boxed squares highlight ω-structured material whose time history is inconsistent with the displacive UZ pathway.

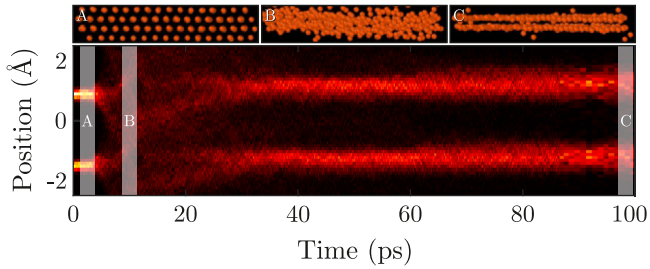

FIG. 12. Linear number density of atoms undergoing diffusive restructuring in a $45 \times 45 \times 8$ Å^3 Lagrangian material element measured along the shock direction (the z axis). Insets A, B, and C show side-on views (along the x axis) of the element 2.5, 10, and 100 ps into the simulation, respectively, highlighting important stages of the $(0001)_\alpha \rightarrow (11\bar{2}0)_\omega$ restructuring.

35% of all atoms have an average neighbor displacement greater than 1.5 Å (approximately half the nearest-neighbor distance); around 10% see at least one of their neighbors wander by distances of 5 Å or more. The diffusive "channel" that operates alongside the conventional displacive one is thus highly active and forms an integral part of the microstructure formation process.

When we compare the morphology of the displacive and diffusive bodies of atoms with that of the final crystal structure [shown in Fig. 11(c)], we observe a strong, but not perfect, correlation. The atoms whose environments transform in a displacive manner are those that assume the ω structure at late times (as expected) while nearly all atoms that suffer diffusive motion constitute the noncrystalline material at the boundaries or interstices between the ω grains. However, this rule does not hold universally: there exist pockets of material near the grain boundaries whose neighbor displacements are inconsistent with the simple displacive motion of the UZ mechanism, yet assume the ω structure nevertheless [see boxed regions in Fig. 11(c)]. To better understand the nondisplacive dynamics in these boundary regions, we illustrate in Fig. 12 the time history of the atomic plane structure in a representative material element. The atomic motion is clearly diffusive. We observe complete disintegration of the $(0001)_\alpha$ basal plane structure over a few picoseconds, followed by a gradual reconstruction of the $(11\bar{2}0)_\omega$ planes due to diffusive motion. Via this mechanism, atoms that stray from the UZ pathway can be "rescued" and allowed to join surface of an ω grain.

Curiously, we find that the diffusive channel does not always yield a perfect ω structure. The volumetric pockets of noncrystalline material visible in Fig. 11(c) that live in the interstices between ω grains are the result of the diffusive channel forming an *ω-like* structure that is pervaded by self-interstitial defect atoms sitting between the $(11\bar{2}0)_\omega$ planes. Thus, the prevailing thermodynamic driving force towards the ω phase via the diffusive channel does not always succeed in creating an ω structure that is defect free. We compare the radial distribution functions (RDFs) of the ω and ω-like material in the Supplemental Material [44]. This ω-like material, which comprises about 5% of the final atomistic configuration by mass, will be examined further in Sec. III B.

To summarize, real-space analysis reveals that the shock-driven $\alpha \rightarrow \omega$ phase transition proceeds via a complex combination of both displacive and diffusive motion. The dominant process is the displacive Usikov-Zilberstein pathway, which involves the formation of an intermediate, short-lived β structure via the Burgers mechanism. The majority of the granddaughter ω grains heterogeneously nucleate at twin boundaries in the transient β nanocrystal via a modified version of the in-plane UZ pathway, and assume the Silcock orientation with respect to the parent α crystal; the remainder transform via the out-of-plane UZ pathway and thus take the TAO-I orientation. Alongside conventional displacive reordering, we observe limited diffusive motion that is initiated at the junctions between β grains and unfolds over tens to hundreds of picoseconds. This channel yields both defect-free and defective ω material, the latter being concentrated at the interstices between ω grains proper and constituting around 5% of the configuration at late times. The ω phase comprises 60% of the mass (of which 95% and 5% assume the Silcock and TAO-I orientations, respectively) and coexists with residual α and β nanocrystals of mass fractions 2% and 5%, respectively. The remaining 28% of the atoms form noncrystalline grain-boundary material.

B. Reciprocal-space analysis

While the real-space analysis in Sec. III A gives us the luxury of examining the $\alpha \rightarrow \omega$ transition in atomistic detail, our understanding of this process is in reality limited to what can be discerned experimentally using ultrafast diagnostics, such as femtosecond x-ray diffraction (XRD). In this section, we will directly compare time-resolved diffraction patterns generated from our simulations with those obtained in dynamic-compression experiments, and interpret their form by examining the computational cell's full three-dimensional structure factor.

The experiment with which we will compare our simulations is described in full in the study of Singh *et al.* [18]; we recap only the essential details here. The laser-driven shock-compression experiments were performed at the Matter in Extreme Conditions (MEC) [57] end station of the Linac Coherent Light Source (LCLS). The authors dynamically compressed single-crystal α-Zr targets of 40-μm thickness along their [0001] axis to pressures of between 5 and 18 GPa, using a 15-ns-long flat-top laser-pulse profile to ensure uniformity of the compressed state. Immediately before the shock front reached the rear surface of the targets, they were probed with a 50-fs burst of collimated 10-keV photons traveling parallel to the target normal (i.e., the original [0001] direction). The resulting time-resolved diffraction patterns were recorded on a set of four Cornell-Stanford Pixel Array Detectors (CSPADs) placed around the beam in a transmission geometry. Here, we focus on a shot taken on an α-Zr target compressed to 15.2 GPa.

In Fig. 13(a), we show a synthetic two-dimensional diffraction pattern generated from our MD simulations at the latest time accessed (0.2 ns after compression begins) expressed in $(2\theta, \phi)$ coordinates, where 2θ is the scattering angle and where ϕ expresses the direction of scattering around the beam axis. The sixfold-symmetric diffraction pattern comprises a discrete set of scattering peaks distributed at regular intervals around a subset of the possible ω-Zr Debye-Scherrer

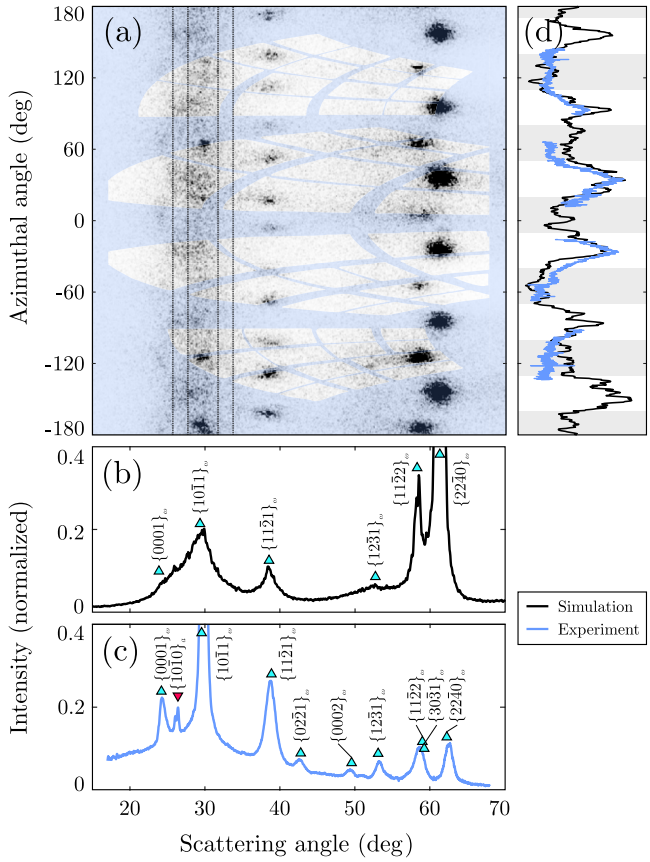

FIG. 13. Comparison of diffraction patterns from [0001]-oriented α-Zr shocked to 15 GPa, generated from MD simulations (black) and obtained in a dynamic-compression experiment (blue) [18], using a 10-keV x-ray beam at normal incidence to the sample. (a) Synthetic 2D diffraction pattern dewarped into $(2\theta, \phi)$ space, with scattering angle 2θ varying horizontally and azimuthal angle ϕ vertically. The mask shows angular regions with no detector coverage in the experiment. (b), (c) Azimuthally averaged diffraction patterns from the simulation and experiment, respectively. Intensities are expressed as a fraction of the maximum peak height. (d) Lineouts showing the average azimuthal variation of the diffuse scattering in the two thin bands centered around $2\theta = 30°$ in (a). Gaps in the experimental signal are caused by incomplete angular coverage of the detectors. Regions of maximal and minimal intensity in the diffuse band are indicated by white and gray bands, respectively.

rings. The clearest rings are the $\{11\bar{2}1\}_\omega$ at $2\theta = 39°$, the $\{11\bar{2}2\}_\omega$ at 59°, and the $\{22\bar{4}0\}_\omega$ (by far the brightest) at 61°. These peaks are primarily generated by the Silcock-oriented ω grains. There also exist several clear $\{10\bar{1}1\}_\omega$ Bragg peaks with irregular ϕ spacings at $2\theta = 30°$, which come from the relatively rare TAO-I-oriented grains. Thus, of all possible reflections from an ω-Zr polycrystal, we observe a highly restricted, discrete set due to the finite number of orientations the UZ pathway allows the ω grains to take.

When compared to the experimental pattern, the Bragg-type parts of the synthetic diffraction are similar in several aspects, and dissimilar in others. We show for reference the azimuthally integrated, one-dimensional patterns at 15 GPa in Figs. 13(b) and 13(c). For rings that are present in both patterns, we have confirmed that the peaks they contain appear at the same azimuthal positions. However, we note that a few reflections seen in the experiment, most notably the extremely strong $\{10\bar{1}1\}_\omega$ peak at 30°, are largely absent in the simulated signal. These reflections are generated by a third set of crystallographic orientations of the ω phase observed by Singh *et al.* that does not appear in our simulations. This, as discussed in Ref. [18], suggests a lack of transferability of the Zong potential, and is perhaps unsurprising given that the atomistic pathway bringing about this third orientation relationship did not feature in this potential's training set.

The second major discrepancy is in the relative heights of the diffraction peaks. For example, while the $\{11\bar{2}2\}_\omega$ and $\{22\bar{4}0\}_\omega$ peaks are present in both the experimental and simulated patterns, they are far stronger in the latter. The discrepancy is owed to the peculiar nature of this particular experiment, in which a quasimonochromatic, collimated x-ray source probes a highly symmetric polycrystal containing only a small set of distinct crystal orientations. In such a scenario, there are, in general, no grains that meet the Bragg condition "exactly"; rather, all Bragg-type diffraction arises from near misses between the Ewald sphere and the maxima in the sample's structure factor. The intensity of such peaks is acutely sensitive to small changes in the crystal structure's density and orientation. It so happens for the present simulation that the $\{22\bar{4}0\}_\omega$ scattering vectors of grains with the Silcock orientation satisfy the Bragg condition almost perfectly (hence the extreme intensity of the $\{22\bar{4}0\}_\omega$ peak), while this is not the case in the experiment, for which the c/a ratio is slightly different (0.605 compared with 0.621). This concept of marginal Bragg diffraction will be developed further shortly.

The feature of the diffraction on which we will focus in this study is not the Bragg-type scattering, but the anomalous diffuse background. In both the experimental and simulated one-dimensional diffraction patterns, we observe a broad band of scattering that is maximal at around $2\theta = 30°$. A casual inspection of this signal might bring to mind either a liquidlike or glasslike state, until one notices its azimuthal structure. As shown in Fig. 13(d), the diffuse band of scattering exhibits clear intensity modulations around the beam with a period of $\Delta\phi = 60°$. The remarkable similarity between the structures of the diffuse band in the experiment and simulation indicates that the simulations may be bearing out the underlying physics correctly.

To better understand the structure of both the Bragg-type and diffuse components of the synthetic diffraction pattern, we have constructed an overview of the simulated specimen's full three-dimensional structure factor in Fig. 14. In Fig. 14(a), we provide pole figures showing the direction of planes in α, β, and ω phases whose associated scattering vectors are of the appropriate magnitude to give scattering in the $2\theta \sim 30°$ region. We indicate in these pole figures the azimuthal regions containing the maxima in the diffuse scattering band by white sectors, and those nearer to minima by gray sectors, analogous to the shading in Fig. 13(d). Vectors at the center of the pole figures are directed along the shock direction, while those on the circumference are orthogonal to it.

We then show in Fig. 14(b) the reciprocal-space locations of these and many other scattering vectors collapsed onto a single plane containing the shock direction and the transverse direction. In this projection, reciprocal lattice vectors are

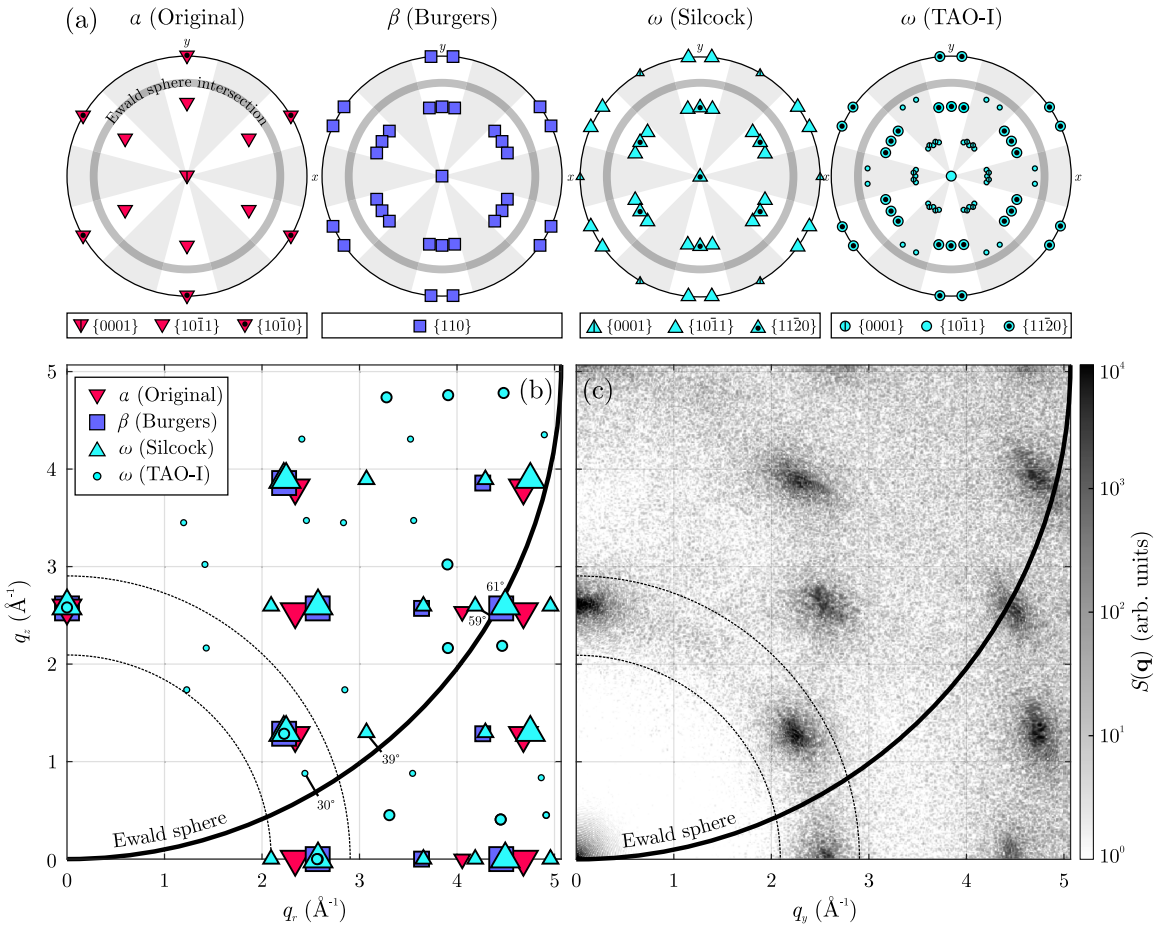

FIG. 14. Overview of the structure factor of the simulated [0001]-oriented α-Zr crystal following the shock-induced $\alpha \rightarrow \omega$ phase transition at 15 GPa. (a) Pole figures showing ideal directions of scattering planes with $\mathbf{q}$ vectors satisfying $2.1 \leqslant \|\mathbf{q}\| \leqslant 2.9\,\text{Å}^{-1}$, including the original [0001]-oriented α single crystal, the 6 distinct β Burgers orientations, the 3 distinct ω Silcock orientations, and the 12 distinct ω TAO-I orientations. Planes whose azimuthal direction falls near the maxima in the sixfold-symmetric diffuse scattering observed in the diffraction pattern (white sectors) are rendered with relatively large symbols; those near the minima (gray sectors) are smaller. Semitransparent rings show the regions intersected by the Ewald sphere (i.e., the regions visible in the diffraction pattern). (b) Collapsed view of reciprocal space showing reciprocal lattice vectors plotted with abscissa $q_r = \sqrt{q_x^2 + q_y^2}$ and ordinate q_z to demonstrate their proximity to the Ewald sphere. Symbols are again differentiated by size according to whether they fall in azimuthal regions containing maxima or minima of the diffuse scattering. Scattering vectors that actively contribute to Bragg-type peaks are connected to the Ewald sphere with their corresponding 2θ angle labeled. Dashed lines indicate loci for which $\|\mathbf{q}\| = 2.1\,\text{Å}^{-1}$ and $2.9\,\text{Å}^{-1}$. (c) True structure factor of the target in the $q_y q_z$ plane (which contains a maximum in the azimuthal modulations). Intensity displayed on a logarithmic scale to expose interpeak structure.

plotted with coordinates

$$(q_r, q_z) = \left(\sqrt{q_x^2 + q_y^2}, q_z\right), \tag{3}$$

such that all points on the same "orbit" around the shock axis appear at the same position. The purpose of this projection is to show the proximity of each reciprocal lattice vector to the Ewald sphere and hence its degree of contribution to the diffraction pattern, for which one only needs to know its cylindrical coordinates q_r and q_z. We differentiate between scattering vectors with different azimuthal positions around the shock direction only by symbol size: those situated in regions nearer the maxima in the diffuse band [i.e., those in white sectors in Fig. 14(a)] are plotted with larger symbols for emphasis, while those nearer the minima [in gray sectors in Fig. 14(b)] have smaller symbols. For clarity, scattering vectors that contribute appreciably to the diffraction pattern due to their proximity to the Ewald sphere are labeled by their corresponding 2θ angle. Together, Figs. 14(a) and 14(b) explain the Bragg-type structure of the diffraction pattern in Fig. 13.

We first reiterate the observation that the Bragg condition is met perfectly almost nowhere. The $\{10\bar{1}1\}_\omega$ peak at 30° from the TAO-I-oriented grains and the $\{11\bar{2}1\}_\omega$ and $\{11\bar{2}2\}_\omega$ peaks at 39° and 58° from the Silcock-oriented grains are all generated by scattering vectors sitting marginally "below" the surface of the Ewald sphere. It is only the $\{22\bar{4}0\}_\omega$ scattering vectors, and, in fact, the $\{220\}_\beta$ vectors, with which they overlap, that satisfy the Bragg condition almost perfectly, leading to its exceptionally strong diffraction peak.

We next note that, with the exception of the $\{10\bar{1}1\}_\omega$ scattering vectors from the TAO-I-oriented grains, the region of reciprocal space in which the diffuse scattering is maximal (namely, the $2\theta \sim 30°$ zone of the Ewald sphere) is devoid

of coherent scattering features. In this region, the Ewald sphere threads its way through a gap flanked by clusters of nearly overlapping reciprocal lattice vectors from the α, β, and ω phases. The cluster outside the Ewald sphere comprises a $\{10\bar{1}0\}_\alpha$ peak along with pairs of $\{110\}_\beta$, $\{10\bar{1}1\}_\omega$, and $\{11\bar{2}0\}_\omega$ vectors, all of which sit at 90° to the shock direction. The cluster inside the Ewald sphere comprises a $\{10\bar{1}1\}_\alpha$ peak along with triplets of almost exactly overlapping $\{110\}_\beta$, $\{10\bar{1}1\}_\omega$, and $\{11\bar{2}0\}_\omega$ peaks inclined at around 60° to the shock direction. As illustrated in the pole figures in Fig. 14(a), the scattering vectors in question fall exclusively in azimuthal regions coinciding with the maxima in the diffuse scattering band. This hints at the possibility that the diffuse signal is the result of the Ewald sphere sampling the tenuous wings of the intensity distribution around these clusters of scattering vectors.

To show this directly, we have plotted in Fig. 14(c) the structure factor of the atomistic configuration calculated from its Fourier transform. The structure factor is shown in the $q_y q_z$ plane, meaning the visible maxima correspond to the reciprocal lattice vectors plotted with larger symbols in Fig. 14(b). We observe that the two previously mentioned clusters of scattering vectors centered approximately at coordinates (2.55, 0) Å^{-1} and (2.25, 1.25) Å^{-1} are connected by a bridge of non-negligible scattering intensity through which the Ewald sphere passes. The value of the structure factor in this diffuse region is 2 to 3 orders of magnitude smaller than at the maxima. Diffuse scattering of this magnitude would ordinarily be eclipsed by coherent scattering from nearby Bragg peaks, were it not for the sparse nature of the target's reciprocal space. What, then, is the origin of the tenuous interpeak scattering intensity?

Several mechanisms can siphon intensity from the crystalline maxima of the structure factor into the space between them. Candidates include (1) the displacement of atoms from their ideal crystal sites due to thermal motion, which causes thermal diffuse scattering (TDS); (2) the presence of extremely small coherently scattering domain sizes, whose reciprocal-space extent is relatively large; and (3) disordering due to high densities of crystal defects. It transpires that all three of these mechanisms contribute to the simulated diffuse scattering signal.

To measure the amount of TDS in our simulations, we compared the structure factor of the original atomistic configuration with that of another configuration obtained by quenching the first, i.e., one whose temperature has been rapidly reduced by a thermostat. We compare the synthetic diffraction of the "hot" (500 K) and "cold" (20 K) configurations in Fig. 15. Here, we have masked out the $\{10\bar{1}1\}_\omega$ peaks from the TAO-I-oriented grains that sit atop the diffuse band to make the latter's shape and magnitude clearer. We observe that while quenching the system leaves the height of the Bragg peaks largely unchanged (in fact, the $\{22\bar{4}0\}_\omega$ peak noticeably *grows* thanks to the reduced Debye-Waller effect), the diffuse signal falls to approximately half of its original value over the entire sampled 2θ range. It should be acknowledged that the phonons in our classical simulations are necessarily distributed according to Maxwell-Boltzmann rather than a Bose-Einstein statistics, and therefore the absolute values of the TDS that our simulations predict should be

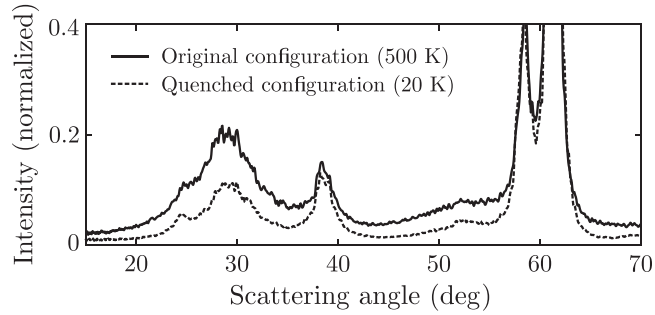

FIG. 15. Synthetic diffraction patterns from [0001]-oriented α-Zr shocked to 15 GPa before and after quenching from the original 500-K shock state to one with a temperature of just 20 K. Both patterns are normalized by the maximum peak height from the 500-K signal. The weak $\{10\bar{1}1\}_\omega$ Bragg peak at 30° has been masked out to make clearer the shape of the diffuse scattering peak sitting below it.

treated with caution. With that said, we note that the simulated TDS accounts for only half of the diffuse signal; even after quenching, there remains a diffuse peak whose integrated intensity is still comparable to that of the Bragg peaks. The remaining nonthermal intensity must be explained either by very small scattering domains (in the form of the residual α and β nanograins), or the presence of material lacking crystalline order.

Cluster analysis of the residual α and β phases (which have mass fractions of 2% and 5%, respectively) reveals that their typical grain diameter is of order $D = 2$–3 nm. The dimension of the shape function dressing each of their scattering vectors is therefore $2\pi/D \sim 0.2 - 0.3\,\text{Å}^{-1}$, a distance comparable to the separation between the above-mentioned clusters of scattering vectors and their points of closest approach on the Ewald sphere. In other words, the Ewald sphere must be sampling non-negligible intensity from α and β nanoparticles' broad structure factor, thus contributing to the (anisotropic) diffuse scattering signal.

Similarly, we identified in Sec. III A pockets of long-lived, defective, ω-like material occupying the interstices between ω grains. That these atoms are relatively poorly ordered suggests their structure factor may be of inherently "lower contrast," with appreciable intensity between the Bragg peaks. To compare the structure of this ω-like material with that of perfect ω in a like-for-like manner, we carved out 50 spherical nanoclusters of each structure from the unquenched atomistic configuration [see Figs. 16(a) and 16(b)], and calculated their structure factors normalized by the total number of atoms sampled. Crucially, the nanoclusters all have the same diameter of 2 nm (clusters of ω-like material larger than this are rare). The identical cluster size means the extrinsic broadening of the structure factor peaks caused by the finite scattering domain size is equivalent, and any remaining broadening must be intrinsic to the atomistic structure.

We compare the structure factors of the ω and noncrystalline ω-like nanoclusters sampled in the $q_y q_z$ plane in Figs. 16(c) and 16(d). The structure factor of the perfect ω clusters has the expected form, namely, a discrete set of points dressed by the oscillatory, spherically symmetric shape functions characteristic of a small, spherical scattering domain.

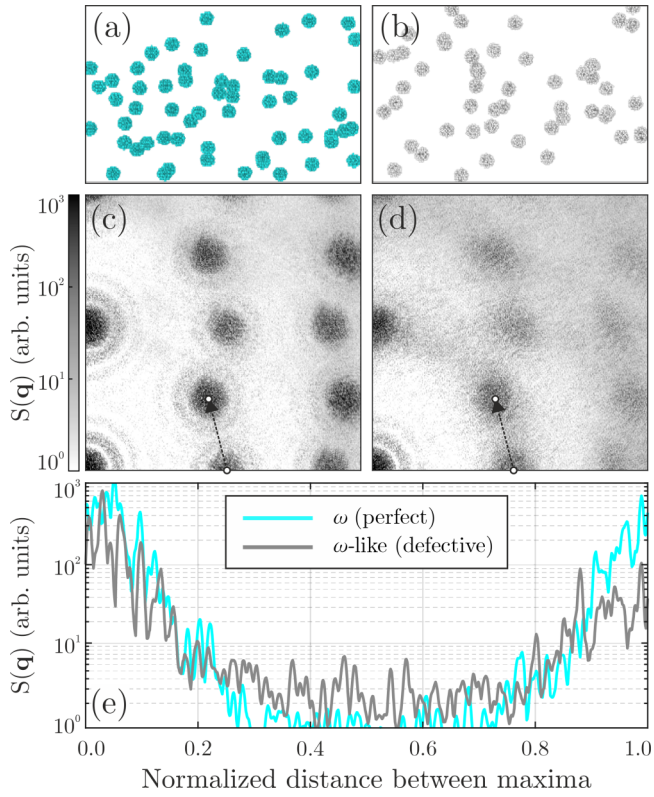

FIG. 16. Comparison of the structure factors of perfect ω and defective ω-like nanoclusters taken from the late-time atomistic configuration. (a), (b) Visualization of the ω and ω-like nanoclusters, respectively, all with a radius of approximately 2 nm. (c), (d) Corresponding structure factors calculated in the $q_y q_z$ plane, displayed on a logarithmic scale. (e) Comparison of the structure factor variation along the path between the maxima indicated by dashed arrows in (c) and (d).

The structure of the defective ω material is qualitatively similar, but is of much lower contrast. The intensity of the peaks diminishes considerably faster with increasing q, and far more intensity is distributed between the peaks. To make this more evident, we show in Fig. 16(e) the intensity variation along the reciprocal-space path shown in Figs. 16(c) and 16(d), which traverses the region whence the diffuse signal comes. While the difference between the coherent and diffuse scattering is a factor of almost 1000 for the ω nanoclusters, it is only 10–100 for the defective material. We speculate that the diffuse scattering seen in the synthetic diffraction patterns arises partially from the tenuous wings of the maxima in the structure factor of the interstitial, partially disordered material.

The question that immediately arises is as follows: What is the relative contribution of the α and β nanoparticles and the interstitial defective nanoclusters to the (nonthermal) diffuse scattering? The natural way to evaluate the contribution of (say) the defective material would seem to be to calculate synthetic diffraction from the disordered nanoclusters in isolation, with all other atoms removed, and to calculate the fraction of diffuse peak it accounts for. In practice, we find that the diffuse feature produced by these defective pockets of material alone is of considerably greater width than the diffuse band from the complete aggregate; the same is true when we isolate the α and β nanoparticles. Indeed, we have made many attempts to additively decompose the diffraction pattern into separate contributions from the ω grains, the partially disordered interstitial material, and the residual α and β grains, and we have invariably failed. The reason is that we cannot assume the positions of atoms in adjacent regions of differing phases are uncorrelated. Looking again at Fig. 14, we see that there are many instances of reciprocal lattice vectors from the α, β, and ω phases overlapping almost exactly. This follows from the shuffle-mediated nature of the $\alpha \rightarrow \beta \rightarrow \omega$ phase transition, which preserves the crystal's planar structure in certain directions despite causing drastic changes in atomic coordination. The clearest instantiation of this effect is the spike of reciprocal-space intensity concentrated at $\mathbf{q} = (0, 0, 2.6)\,\text{Å}^{-1}$, which represents a near-perfect overlap of the $(0001)_\alpha$, $(011)_\beta$, $(11\bar{2}0)_\omega$ (Silcock), and $(10\bar{1}1)_\omega$ (TAO-I) scattering vectors; to ignore coherence and treat the aggregate peak as a linear superposition of peaks from individual phases would be incorrect. In a similar vein, correlations between the positions of atoms in the ω grains and those of the partially disordered ω-like pockets between them cannot be ignored. These phases (if the ω-like material can be described as such) are contiguous, and have structures differing only by the presence or absence of point defects. It therefore does not make sense to treat the two subsets of atoms as independent scattering bodies; one can only speak of scattering from their aggregation.

For these reasons, we cannot partition the nonthermal component of the diffuse scattering into contributions from defective, partially disordered material and from the nanoscale α and β grains that survive the transition process, and we further contend that doing so is impossible; while both effects surely contribute, they do so nonlinearly. It is only with an atomistic simulation technique such as molecular dynamics that the minutiae of the correlations between atomic positions in the various daughter phases, and their effect on the form of the diffuse scattering signal, can be faithfully modeled.

The final point we shall make is that it is largely by virtue of the specimen's sparse reciprocal space that the anisotropic diffuse scattering is so conspicuous. We previously suggested that the relatively weak diffuse signal would be obscured by conventional Bragg-type scattering for the kind of polycrystalline samples more regularly used in femtosecond x-ray diffraction experiments. To generate a representative diffraction pattern from a powderlike sample without simulating a true polycrystal under dynamic compression (which would be exorbitantly expensive under the present potential), we take the full three-dimensional structure factor from our single-crystal simulations, $S(\mathbf{q})$, and calculate its one-dimensional polycrystalline analog using an unweighted spherical average:

$$\langle S \rangle(q) = \frac{1}{4\pi} \int d\Omega\, S(\mathbf{q})\,. \tag{4}$$

The resulting structure factor is that of an ensemble of independently scattering replicas of our final configuration with an isotropic orientation distribution. By taking this average, we implicitly assume that every parent α crystallite, no matter its initial orientation with respect to the compression direction, reaches a shock state with an identical (albeit rotated) microstructure, which would almost certainly not be the case

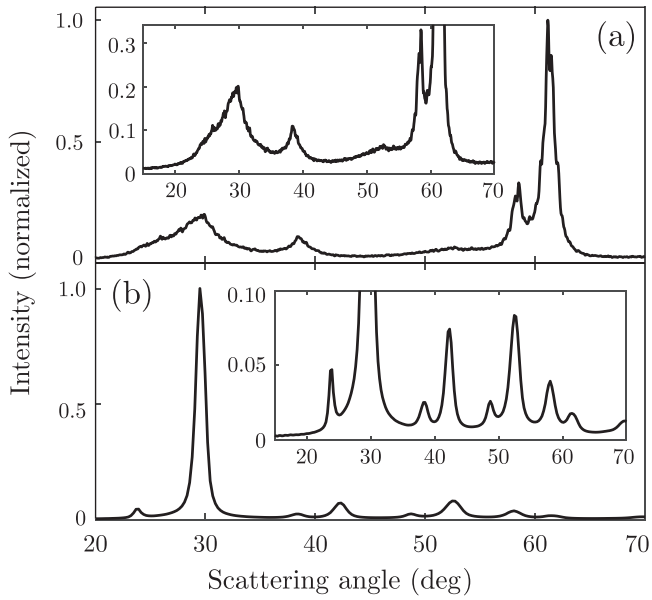

FIG. 17. Comparison of synthetic diffraction patterns of (a) the original, initially monocrystalline atomistic configuration and (b) a powderlike polycrystalline analog obtained by spherical averaging of the former configuration's structure factor. Insets show closer views of the lower-intensity peaks for each configuration. Intensities are expressed as a fraction of the maximum peak height.

in reality. We do not believe this detail is important for the purposes of the comparison we wish to make, as it is only the leading-order relative intensities of the Bragg-type and diffuse scattering that matter.

Figure 17 compares the azimuthally integrated diffraction patterns from the original single-crystal shock-MD simulation with that of a polycrystalline analog. The difference is stark. In the former case, the $\{22\bar{4}0\}_\omega$ at $2\theta = 61^\circ$ dominates the landscape, and the diffuse peak centered at 30°, while of far lower maximal intensity, is clearly resolvable and of a comparable integrated intensity. For the polycrystalline analog, meanwhile, all other reflections are dwarfed by an exceptionally intense Bragg peak at 29°, which is in fact a combination of closely overlapping $\{10\bar{1}1\}_\omega$ and $\{11\bar{2}0\}_\omega$ Debye-Scherrer rings. Resolving a weak diffuse peak beneath the towering $\{10\bar{1}1\}_\omega/\{11\bar{2}0\}_\omega$ Bragg peak would be extremely difficult without strong prior constraints on the latter's line shape. We therefore maintain that the anisotropic diffuse scattering signal is visible thanks to the single-crystal nature of the target. This concept will be discussed further in Sec. IV.

In summary, we have generated synthetic diffraction patterns from [0001]-oriented single-crystal α-Zr shock compressed to 15 GPa following the $\alpha \rightarrow \omega$ phase transition using a 10-keV x-ray beam at normal incidence to the simulated target. In addition to a subset of the full complement of ω diffraction peaks, we observe an anisotropic diffuse scattering signal centered at $2\theta = 30^\circ$ with sixfold rotational symmetry around incident beam direction, much like that observed by Singh *et al.* in an analogous dynamic-compression experiment [18]. The (classical) simulations suggest that approximately half of the diffuse signal arises from thermal diffuse scattering, while the remainder is generated by a combination of interstitial, defective ω-like material and residual, nanoscale α and β grains that survive the transition. We show that the diffuse peak would likely be obscured by conventional Bragg-type scattering were the target's initial texture to be polycrystalline.

IV. DISCUSSION

While the present computational study makes a number of interesting predictions about the physics of zirconium under dynamic compression, we believe its most important predictions pertain to the peculiarities of the single-crystal diffraction configuration. The [0001]-oriented α-Zr single crystals used in the experimental study of Singh *et al.* [18] that we simulate here possess the strongest starting texture possible. In other words, their reciprocal space is populated by a sparse set of extremely localized scattering vectors, and is otherwise entirely empty. Such targets are therefore virtually guaranteed not to satisfy the Bragg condition when illuminated by a collimated, quasimonochromatic x-ray source. We have shown that even following the Usikov-Zilberstein-mediated $\alpha \rightarrow \omega$ phase transition, which creates β- and ω-Zr grains with 6 and 15 distinct orientations, respectively, the specimen's reciprocal space remains sparse in real terms. By this, we mean that the Bragg condition is exactly satisfied virtually nowhere, except when the combination of shock-induced strains and rotations happens to map a scattering vector onto the Ewald sphere. We observed this behavior in the $\{22\bar{4}0\}_\omega$ peak at 15 GPa, but changing the shock pressure even slightly could displace this scattering vector from the Ewald sphere and thus largely extinguish its Bragg peak. The majority of the diffraction peaks are generated by scattering vectors that miss the Ewald sphere by varying degrees.

The consequence of the target's sparse reciprocal space is that the overall intensity scale of the diffraction is vastly reduced, and the off-Bragg, diffuse elements of the diffraction pattern that might ordinarily be overlooked (or even subtracted off as a background) suddenly come to the fore. By way of comparison, we approximated the diffraction pattern generated by a powderlike polycrystalline Zr target, and demonstrated that the diffuse peak at 30° would likely be buried beneath the wings of the "true" Bragg peaks. This appears to account for the fact that the diffuse features observed in our simulations are also observed in the single-crystal study of Singh *et al.*, but *not* in analogous experiments performed using polycrystals [18]. To reiterate, it not necessarily the case that the diffuse scattering in this configuration is particularly "strong"; rather, the Bragg scattering is "weak." Note that this phenomenon is by no means peculiar to zirconium; one could reasonably expect that diffuse scattering of a qualitatively similar nature might be observable in *any* single crystal whose texture is substantively diversified by dynamic compression.

With that being said, there are aspects of the present experiment that make the diffuse signal more conspicuous. First, the fact that the diagnostic x-ray beam travels at normal incidence to the target normal, which is to say, parallel to the target's initial axis of sixfold symmetry, is not unimportant. The orientation (and radius) of the Ewald sphere is such that its $2\theta \sim 30^\circ$ zone exclusively samples regions of particularly strong diffuse scattering that appear every $\Delta\phi = 60^\circ$ around

its surface. These regions are largely devoid of coherent scattering features (with the exception of the $\{10\bar{1}1\}_\omega$ from the TAO-I-oriented grains) and moreover correspond to relatively modest Bragg and emergence angles, such that attenuation due to the atomic-form and self-attenuation factors in this zone is weak. These effects conspire to give a clearly defined diffuse signal that becomes clearer yet after azimuthal averaging. Bringing the x rays in at a nonzero incidence angle would break the diffraction pattern's sixfold rotational symmetry and thus blur the structure of the diffuse scattering. Tilting the Ewald sphere would also increase the "probability" of one or more of the multitude of scattering vectors satisfying $\|\mathbf{q}\| \sim 2.5\ \text{Å}^{-1}$ meeting the Bragg condition and thus overshadowing the diffuse signal.

Second, the molecular dynamics simulations suggest that α-Zr dynamically compressed along [0001] contains microstructures that generate anisotropic diffuse scattering over and above conventional thermal diffuse scattering. Under the Zong potential, the $\alpha \rightarrow \omega$ phase transition is realized primarily via the displacive Usikov-Zilberstein mechanism, which, as described in Sec. III A, brings about the formation of a short-lived, extremely fine β-Zr nanocrystal. The atomistic disorder fomented at the incoherent boundaries between the β nanograins ultimately leads to the diffusive formation of pockets of defective ω-like material whose structure factor is characterized by non-negligible intensity between the peaks. The simulations further suggest that a subset of the β grains is kinetically inhibited from completing the transformation to the ω phase (over the 0.2-ns simulation timescale, at least), and that these minuscule grains act as an additional source of relatively delocalized diffraction. Within the classical framework of the simulations, the thermal and nonthermal parts of the diffuse scattering are of almost equal strength.

An essential question is whether the diffuse signal can be used to diagnose the dynamically compressed target's Hugoniot state: the thermal component is directly linked to the system's temperature, the nonthermal component to the mesoscale structure and defect content. Despite our best efforts, we have found that it is not possible to additively decompose the nonthermal diffuse scattering into contributions from the residual α and β grains and from the defective ω-like material. Furthermore, although the thermal diffuse scattering *is* apparently separable, its structure is very similar to that of the nonthermal diffuse scattering. To "invert" the diffuse signal and decompose it into its constituent parts is, therefore, not a trivial task. Molecular dynamics simulations do at least allow us to model the diffuse scattering in a forward sense and to check for consistency with experimental data. Indeed, we believe atomistic simulation techniques are *required* to faithfully model diffuse scattering of the kind observed here, as they automatically incorporate the subtleties of atom-atom correlations within and between different phases in a way that mesoscale or continuum-scale models usually do not.

Of course, the fidelity of these simulations depends on the interatomic potential they use. We have shown that the Zong potential [35] bears out several salient features of the experimental data. It successfully produces a shock-induced $\alpha \rightarrow \omega$ phase transition at similar pressures to those measured experimentally, and in fact produces Silcock- and TAO-I-oriented ω grains in approximately the correct proportion. As we have seen, it also predicts a diffuse diffraction signal with an azimuthal structure identical to that seen in experiment. However, the Zong potential also has shortcomings. On an "idealistic" level, the fact that it is not everywhere continuous is obviously troubling. The consequences of the jumps in the potential energy surface are not catastrophic, but surely have a subtle influence on the system's dynamics that the user cannot easily quantify. There is a more "pragmatic" issue with the Zong potential, however, which is that it fails to reproduce one of the three $\alpha \rightarrow \omega$ transition mechanisms observed by Singh *et al.* [18].

The atomistic pathway associated with this mechanism (which was not known at the time of the potential's creation, and, indeed, remains unknown at the time of writing) did not form part of the *ab initio* energy database on which the potential was trained. It appears that the Zong potential (whose mathematical form is essentially aphysical) is unable to correctly extrapolate the potential energy surface into that unmapped region of configuration space. This is reflective of a more general observation made about machine-learning-class potentials by Nicholls *et al.* [45], namely, that they excel in the physical domain for which they are specifically trained, but often exhibit little to no transferability beyond this domain. Thus, there is a pressing need to identify the $\alpha \rightarrow \omega$ atomistic pathway associated with the third ω variant observed by Singh *et al.* [18], and to incorporate its associated configuration space into the training set of a new and physically robust potential for zirconium.

Finally, we note that much of the rich postshock microstructure that the simulations predict, including the residual, kinetically stabilized nanograins and interstitial defective material, is contingent on the existence of the transient intermediate β phase. Were the $\alpha \rightarrow \omega$ transition to occur directly, rather than via the two-stage Usikov-Zilberstein mechanism, we speculate that the resulting Hugoniot state might instead be a relatively "pure" ω nanocrystal that generates comparatively little nonthermal diffuse scattering. Experimental evidence for the intermediate β phase in dynamically compressed Zr does indeed exist. Armstrong *et al.* reported direct observation of metastable β-Zr using *in situ* x-ray diffraction timed only hundreds of picoseconds after the onset of compression [31]. In their nanosecond-duration experiments, Singh *et al.* also showed that there existed weak diffraction peaks whose locations were consistent with a small phase fraction of residual β-Zr [18]. For these reasons, we see no reason to doubt the predicted formation of the transient β phase and all the attendant microstructure responsible for the nonthermal diffuse scattering.

V. CONCLUSION

We have performed large-scale classical molecular dynamics simulations of [0001]-oriented single-crystal zirconium under dynamic uniaxial compression to 15 GPa using a machine-learning-class interatomic potential. The simulations predict a pressure-induced $\alpha \rightarrow \omega$ phase transition mediated primarily via a modified form of the displacive Usikov-Zilberstein mechanism, wherein ω grains heterogeneously nucleate at the twin boundaries of a short-lived intermediate β phase. We further observe diffusive motion initiated at the

junctions between β grains, which leads ultimately to the formation of highly defective ω-like material at the interstices between ω grains.

We generated synthetic diffraction patterns from the simulated late-time atomistic configuration and compared its structure directly with that of femtosecond diffraction patterns acquired in dynamic-compression experiments. Both simulation and experiment revealed a sixfold-symmetric, azimuthally structured diffuse scattering signal beneath the conventional Bragg-type diffraction pattern. The simulations indicate that the anisotropic diffuse scattering stems from a confluence of thermal diffuse scattering, nanoparticlelike scattering from residual α and β grains that survive the phase transition, and from the diffuse scattering components of the interstitial defective material. We demonstrated that the sparse nature of the monocrystalline target's reciprocal space is essential for the observation of the structured diffuse scattering.

These results demonstrate the interpretative power of atomistic simulation techniques in the field of dynamic compression, and underscore the importance of seeking direct, like-for-like comparisons between synthetic and experimental diffraction data. Diffuse scattering from dynamically loaded metals may yet prove to be a novel diagnostic of temperature and microstructure in which atomistic modeling techniques will play an essential role.

ACKNOWLEDGMENTS

The authors would like to express their gratitude to H. Zong and G. J. Ackland for sharing the interatomic potential used to execute the documented simulations. The authors also thank J. S. Wark, P. Svensson, and P. A. Burr for the insights they offered during the development of this work. This research was supported by the Laboratory Directed Research and Development (LDRD) Program at Lawrence Livermore National Laboratory (LLNL) (Projects No. 17-ERD-014 and No. 21-ERD-032). This work was performed under the auspices of the U.S. Department of Energy by LLNL under Contract No. DE-AC52-07NA2734. P.G.H. gratefully acknowledges the support of AWE via the Oxford Centre for High Energy Density Science (OxCHEDS), and further support from EPSRC under Grant No. EP/X031624/1.

[1] S. M. Sharma, S. J. Turneaure, J. M. Winey, and Y. M. Gupta, Transformation of shock-compressed copper to the body-centered-cubic structure at 180 GPa, Phys. Rev. B **102**, 020103(R) (2020).

[2] S. M. Sharma, S. J. Turneaure, J. M. Winey, and Y. M. Gupta, What determines the fcc-bcc structural transformation in shock compressed noble metals? Phys. Rev. Lett. **124**, 235701 (2020).

[3] S. M. Sharma, S. J. Turneaure, J. M. Winey, Y. Li, P. Rigg, A. Schuman, N. Sinclair, Y. Toyoda, X. Wang, N. Weir, J. Zhang, and Y. M. Gupta, Structural transformation and melting in gold shock compressed to 355 GPa, Phys. Rev. Lett. **123**, 045702 (2019).

[4] R. Briggs, F. Coppari, M. G. Gorman, R. F. Smith, S. J. Tracy, A. L. Coleman, A. Fernandez-Pañella, M. Millot, J. H. Eggert, and D. E. Fratanduono, Measurement of body-centered cubic gold and melting under shock compression, Phys. Rev. Lett. **123**, 045701 (2019).

[5] H. Xia, S. J. Duclos, A. L. Ruoff, and Y. K. Vohra, New high-pressure phase transition in zirconium metal, Phys. Rev. Lett. **64**, 204 (1990).

[6] H. Xia, G. Parthasarathy, H. Luo, Y. K. Vohra, and A. L. Ruoff, Crystal structures of group IVa metals at ultrahigh pressures, Phys. Rev. B **42**, 6736 (1990).

[7] J. C. Jamieson, Crystal structures at high pressures of metallic modifications of silicon and germanium, Science **139**, 762 (1963).

[8] M. I. McMahon and R. J. Nelmes, New high-pressure phase of Si, Phys. Rev. B **47**, 8337 (1993).

[9] H. Olijnyk, S. Sikka, and W. Holzapfel, Structural phase transitions in Si and Ge under pressures up to 50 GPa, Phys. Lett. A **103**, 137 (1984).

[10] E. E. McBride, A. Krygier, A. Ehnes, E. Galtier, M. Harmand, Z. Konôpková, H. J. Lee, H.-P. Liermann, B. Nagler, A. Pelka, M. Rödel, A. Schropp, R. F. Smith, C. Spindloe, D. Swift, F. Tavella, S. Toleikis, T. Tschentscher, J. S. Wark, and A. Higginbotham, Phase transition lowering in dynamically compressed silicon, Nat. Phys. **15**, 89 (2019).

[11] A. Lazicki, D. McGonegle, J. R. Rygg, D. G. Braun, D. C. Swift, M. G. Gorman, R. F. Smith, P. G. Heighway, A. Higginbotham, M. J. Suggit, D. E. Fratanduono, F. Coppari, C. E. Wehrenberg, R. G. Kraus, D. Erskine, J. V. Bernier, J. M. McNaney, R. E. Rudd, G. W. Collins, J. H. Eggert, and J. S. Wark, Metastability of diamond ramp-compressed to 2 terapascals, Nature (London) **589**, 532 (2021).

[12] J. Shi, Z. Liang, J. Wang, S. Pan, C. Ding, Y. Wang, H.-T. Wang, D. Xing, and J. Sun, Double-shock compression pathways from diamond to BC8 carbon, Phys. Rev. Lett. **131**, 146101 (2023).

[13] K. Nguyen-Cong, J. T. Willman, J. M. Gonzalez, A. S. Williams, A. B. Belonoshko, S. G. Moore, A. P. Thompson, M. A. Wood, J. H. Eggert, M. Millot, L. A. Zepeda-Ruiz, and I. I. Oleynik, Extreme metastability of diamond and its transformation to the BC8 post-diamond phase of carbon, J. Phys. Chem. Lett. **15**, 1152 (2024).

[14] M. G. Gorman, D. McGonegle, R. F. Smith, S. Singh, T. Jenkins, R. S. McWilliams *et al.*, Shock compression experiments using the DiPOLE 100-X laser on the high energy density instrument at the European x-ray free electron laser: Quantitative structural analysis of liquid Sn, J. Appl. Phys. **135**, 165902 (2024).

[15] J. Hawreliak, J. D. Colvin, J. H. Eggert, D. H. Kalantar, H. E. Lorenzana, J. S. Stölken, H. M. Davies, T. C. Germann, B. L. Holian, K. Kadau, P. S. Lomdahl, A. Higginbotham, K. Rosolankova, J. Sheppard, and J. S. Wark, Analysis of the x-ray diffraction signal for the α-ϵ transition in shock-compressed iron: Simulation and experiment, Phys. Rev. B **74**, 184107 (2006).

[16] S. Pandolfi, S. B. Brown, P. G. Stubley, A. Higginbotham, C. A. Bolme, H. J. Lee, B. Nagler, E. Galtier, R. L. Sandberg, W.

Yang, W. L. Mao, J. S. Wark, and A. E. Gleason, Atomistic deformation mechanism of silicon under laser-driven shock compression, Nat. Commun. **13**, 5535 (2022).

[17] M. Sims, R. Briggs, T. J. Volz, S. Singh, S. Hamel, A. L. Coleman, F. Coppari, D. J. Erskine, M. G. Gorman, B. Sadigh, J. Belof, J. H. Eggert, R. F. Smith, and J. K. Wicks, Experimental and theoretical examination of shock-compressed copper through the fcc to bcc to melt phase transitions, J. Appl. Phys. **132**, 075902 (2022).

[18] S. Singh, M. G. Gorman, P. G. Heighway, J. V. Bernier, D. McGonegle, H. J. Lee, B. Nagler, J. H. Eggert, and R. F. Smith, companion paper, Unexpected observation of disorder and multiple phase-transition pathways in shock-compressed Zr, Phys. Rev. Lett. **133**, 096101 (2024).

[19] S. G. Song and G. T. G. III, Microscopic and crystallographic aspects of retained omega phase in shock-loaded zirconium and its formation mechanism, Philos. Mag. A **71**, 275 (1995).

[20] G. Jyoti, K. Joshi, S. C. Gupta, and S. Sikka, Alpha omicro crystallography of the transition in shock-loaded zirconium, Philos. Mag. Lett. **75**, 291 (1997).

[21] G. Jyoti, R. Tewari, K. Joshi, D. Srivastava, G. Dey, S. Gupta, S. Sikka, and S. Banerjee, Alpha to omega transition in shock compressed zirconium: Crystallographic aspects, in *Phase Transformation and Diffusion*, Defect and Diffusion Forum, Vol. 279 (Trans Tech Publications, Stafa-Zurich, Switzerland, 2008), pp. 133–138.

[22] J. M. Silcock, An X-ray examination of the to phase in TiV, TiMo and TiCr alloys Examen aux rayons x de la phase dans les alliages TiV, TiMo et TiCrEine rntgen-untersuchung der -phase in TiV, TiMo und TiCr legierungen, Acta Metall. **6**, 481 (1958).

[23] G. Sargent and H. Conrad, Formation of the omega phase in titanium by hydrostatic pressure soaking, Mater. Sci. Eng. **7**, 220 (1971).

[24] A. Rabinkin, M. Talianker, and O. Botstein, Crystallography and a model of the $\alpha \rightarrow \omega$ phase transformation in zirconium, Acta Metall. **29**, 691 (1981).

[25] H.-R. Wenk, P. Kaercher, W. Kanitpanyacharoen, E. Zepeda-Alarcon, and Y. Wang, Orientation relations during the α-ω phase transition of zirconium: *In situ* texture observations at high pressure and temperature, Phys. Rev. Lett. **111**, 195701 (2013).

[26] N. Adachi, Y. Todaka, H. Suzuki, and M. Umemoto, Orientation relationship between $\alpha-$phase and high-pressure $\omega-$phase of pure group IV transition metals, Scr. Mater. **98**, 1 (2015).

[27] H. Wang, W. Dmowski, Z. Wang, J. Qiang, K. Tsuchiya, Y. Yokoyama, H. Bei, and T. Egami, Transformation pathway from alpha to omega and texture evolution in Zr via high-pressure torsion, Appl. Phys. Lett. **114**, 061903 (2019).

[28] M. P. Usikov and V. A. Zilbershtein, The orientation relationship between the α- and ω-phases of titanium and zirconium, Phys. Status Solidi A **19**, 53 (1973).

[29] A. R. Kutsar, I. V. Lyasotski, A. M. Podurets, and A. F. Sanches-bolinches, Omega phase of zirconium: Formation under shock wave compression and stability at atmospheric pressure, High Press. Res. **4**, 475 (1990).

[30] T. D. Swinburne, M. G. Glavicic, K. M. Rahman, N. G. Jones, J. Coakley, D. E. Eakins, T. G. White, V. Tong, D. Milathianaki, G. J. Williams, D. Rugg, A. P. Sutton, and D. Dye, Picosecond dynamics of a shock-driven displacive phase transformation in Zr, Phys. Rev. B **93**, 144119 (2016).

[31] M. R. Armstrong, H. B. Radousky, R. A. Austin, E. Stavrou, H. Zong, G. J. Ackland, S. Brown, J. C. Crowhurst, A. E. Gleason, E. Granados, P. Grivickas, N. Holtgrewe, H. J. Lee, T. T. Li, S. Lobanov, J. T. McKeown, B. Nagler, I. Nam, A. J. Nelson, V. Prakapenka *et al.*, Observation of fundamental mechanisms in compression-induced phase transformations using ultrafast x-ray diffraction, JOM **73**, 2185 (2021).

[32] J. Zhang, Y. Zhao, C. Pantea, J. Qian, L. L. Daemen, P. A. Rigg, R. S. Hixson, C. W. Greeff, G. T. Gray, Y. Yang, L. Wang, Y. Wang, and T. Uchida, Experimental constraints on the phase diagram of elemental zirconium, J. Phys. Chem. Solids **66**, 1213 (2005).

[33] C. W. Greeff, Phase changes and the equation of state of Zr, Modell. Simul. Mater. Sci. Eng. **13**, 1015 (2005).

[34] P. Chirkov, G. Eltsov, A. Karavaev, V. Dremov, and A. Mirzoev, Zirconium phase diagram from *ab initio* molecular dynamics, Comput. Mater. Sci. **241**, 113057 (2024).

[35] H. Zong, G. Pilania, X. Ding, G. J. Ackland, and T. Lookman, Developing an interatomic potential for martensitic phase transformations in zirconium by machine learning, npj Comput. Mater. **4**, 48 (2018).

[36] D. Smirnova and S. Starikov, An interatomic potential for simulation of Zr-Nb system, Comput. Mater. Sci. **129**, 259 (2017).

[37] M. S. Nitol, D. E. Dickel, and C. D. Barrett, Machine learning models for predictive materials science from fundamental physics: An application to titanium and zirconium, Acta Mater. **224**, 117347 (2022).

[38] A. Seko, A. Takahashi, and I. Tanaka, First-principles interatomic potentials for ten elemental metals via compressed sensing, Phys. Rev. B **92**, 054113 (2015).

[39] J. S. Smith, O. Isayev, and A. E. Roitberg, ANI-1: an extensible neural network potential with DFT accuracy at force field computational cost, Chem. Sci. **8**, 3192 (2017).

[40] H. Mori and T. Ozaki, Neural network atomic potential to investigate the dislocation dynamics in bcc iron, Phys. Rev. Mater. **4**, 040601(R) (2020).

[41] M. S. Nitol, K. Dang, S. J. Fensin, M. I. Baskes, D. E. Dickel, and C. D. Barrett, Hybrid interatomic potential for Sn, Phys. Rev. Mater. **7**, 043601 (2023).

[42] H. Zong, Y. Luo, X. Ding, T. Lookman, and G. J. Ackland, hcp $\rightarrow \omega$ phase transition mechanisms in shocked zirconium: A machine learning based atomic simulation study, Acta Mater. **162**, 126 (2019).

[43] H. Zong, P. He, X. Ding, and G. J. Ackland, Nucleation mechanism for hcp $\rightarrow$ bcc phase transformation in shock-compressed Zr, Phys. Rev. B **101**, 144105 (2020).

[44] See Supplemental Material at http://link.aps.org/supplemental/10.1103/PhysRevB.110.054113 for the calculation of the theoretical Zr Hugoniot; an illustration of the discontinuities in the Zong potential; a comparison of shock-MD simulations performed with and without the iterative "grow-and-prune" scheme; the method used to control the speed of the second confining momentum mirror; an estimation of the computational speedup offered by the grow-and-prune scheme; a detailed description of the phase-partitioning algorithm; and radial distribution functions of the high-pressure structures formed under shock.

[45] O. G. Nicholls, D. G. Frost, V. Tuli, J. Smutna, M. R. Wenman, and P. A. Burr, Transferability of Zr-Zr interatomic potentials, J. Nucl. Mater. **584**, 154391 (2023).

[46] A. P. Thompson, H. M. Aktulga, R. Berger, D. S. Bolintineanu, W. M. Brown, P. S. Crozier, P. J. in 't Veld, A. Kohlmeyer, S. G. Moore, T. D. Nguyen, R. Shan, M. J. Stevens, J. Tranchida, C. Trott, and S. J. Plimpton, LAMMPS - a flexible simulation tool for particle-based materials modeling at the atomic, meso, and continuum scales, Comput. Phys. Commun. **271**, 108171 (2022).

[47] R. Ravelo, B. L. Holian, T. C. Germann, and P. S. Lomdahl, Constant-stress Hugoniostat method for following the dynamical evolution of shocked matter, Phys. Rev. B **70**, 014103 (2004).

[48] E. J. Reed, L. E. Fried, and J. D. Joannopoulos, A method for tractable dynamical studies of single and double shock compression, Phys. Rev. Lett. **90**, 235503 (2003).

[49] V. V. Zhakhovsky, M. M. Budzevich, N. A. Inogamov, I. I. Oleynik, and C. T. White, Two-zone elastic-plastic single shock waves in solids, Phys. Rev. Lett. **107**, 135502 (2011).

[50] M. I. Mendelev and G. J. Ackland, Development of an interatomic potential for the simulation of phase transformations in zirconium, Philos. Mag. Lett. **87**, 349 (2007).

[51] G. J. Ackland and A. P. Jones, Applications of local crystal structure measures in experiment and simulation, Phys. Rev. B **73**, 054104 (2006).

[52] A. Stukowski, Structure identification methods for atomistic simulations of crystalline materials, Modell. Simul. Mater. Sci. Eng. **20**, 045021 (2012).

[53] P. G. Heighway, D. McGonegle, N. Park, A. Higginbotham, and J. S. Wark, Molecular dynamics simulations of grain interactions in shock-compressed highly textured columnar nanocrystals, Phys. Rev. Mater. **3**, 083602 (2019).

[54] A. Higginbotham, M. J. Suggit, E. M. Bringa, P. Erhart, J. A. Hawreliak, G. Mogni, N. Park, B. A. Remington, and J. S. Wark, Molecular dynamics simulations of shock-induced deformation twinning of a body-centered-cubic metal, Phys. Rev. B **88**, 104105 (2013).

[55] A. Stukowski, Visualization and analysis of atomistic simulation data with OVITO - the Open Visualization Tool, Modell. Simul. Mater. Sci. Eng. **18**, 015012 (2010).

[56] W. Burgers, On the process of transition of the cubic-body-centered modification into the hexagonal-close-packed modification of zirconium, Physica (Amsterdam) **1**, 561 (1934).

[57] B. Nagler, B. Arnold, G. Bouchard, R. F. Boyce, R. M. Boyce, A. Callen, M. Campell, R. Curiel, E. Galtier, J. Garofoli, E. Granados, J. Hastings, G. Hays, P. Heimann, R. W. Lee, D. Milathianaki, L. Plummer, A. Schropp, A. Wallace, M. Welch *et al.*, The matter in extreme conditions instrument at the Linac coherent light source, J. Synchrotron Radiat. **22**, 520 (2015).